Multi-epoch VLBI mapping of the globular cluster M15
A pulsar proper motion analysis

Masterarbeit in Astrophysik von

Franz Kirsten

angefertigt im Institut

Argelander Institut für Astronomie

vorgelegt der

Mathematisch-Naturwissenschaftlichen Fakultät der Universität Bonn

August 2011

Betreuer: Dr. Wouter Vlemmings

1. Gutachter:
Prof. Dr. Michael Kramer

2. Gutachter:
Prof. Dr. Norbert Langer

Contents

1 Introduction

Globular cluster are almost spherical stellar systems composed of up to 10^6 stars within a radius of only a few tens of parsec. They are gravitationally tightly bound objects that can be found mostly throughout the halo and in the bulge of galaxies. Measurements of their metallicity have revealed that they are among the oldest stellar systems in the universe having metallicities down to less than 1 per cent of the solar value (e.g. Koch & McWilliam 2011). Consequently, globular clusters (GC) are of great interest for evolutionary models of star formation. On the other hand, their high age also implies that GCs should host a large number of stars at a very late stage of their evolution a few of which – considering the high stellar density in a GC – are very likely to have undergone encounters with other stars at some point in their lifetime.

This thesis deals with observations of one type of remnant of once massive stars: neutron stars that are observable as pulsars. Any massive stars that were formed during the early stages of a GC's evolution will have already ended their life in a core collapse supernova leaving behind a remnant. Depending on the initial mass of such stars the remnant will either be a black hole or a neutron star (NS). Neutron stars are the most densely packed objects known to exist. Their central density exceeds that of atomic nuclei by a factor of 2 to 3 making them especially interesting for particle physics and the equation of state of matter under such conditions. Essentially, neutron stars are dead stars that emit no energy through nuclear fusion which would make them detectable like ordinary stars. Instead, they need to either be accreting matter from, e.g., a companion star which makes them visible as an X-ray source. Most commonly, however, they are detected in the radio regime as pulsars – objects that appear to emit radiation in a non-continuous manner but in a pulsed way with very stable pulsation periods between a few milliseconds and up to ten seconds. These pulsars are highly magnetized neutron stars whose beam of emission only strikes the observer at intervals equal to the rotation period of the emitting object.

As such, pulsars are very accurate clocks that can be used to perform many very different kinds of astrophysical experiments. The most obvious of those is the determination of the gravitational force needed to keep the NS from disrupting due to its high rotational velocity. More sophisticated applications of pulsars as clocks are based on pulsar timing (Chapter 2.3) and include, e.g., the measurement of binary orbits and tests of General Relativity. Currently, pulsars are the most promising objects to be used in the search for Gravitational Waves (GWs). Such waves distort space-time and, thus, also influence the time of arrival of pulses from a pulsar. In a large network of pulsars the propagation of GWs should be detectable. Most useful for such high precision timing experiments are the millisecond pulsars (MSPs) which have rotation periods of only a few milliseconds. For a MSP to form, a pulsar needs to undergo an evolution involving a companion star at some point of its lifetime. Therefore, it is only natural that MSPs are usually bound in a binary system that itself is part of a globular cluster where the stellar density is high enough to ensure frequent stellar encounters. Consequently, the objects with the highest probability to host MSPs are globular clusters.

Traditionally, pulsars are observed and searched for with single dish radio telescopes. Since the angular resolution of a telescope with diameter D observing at wavelength λ scales as λ/D even the largest single dish radio telescope (the Arecibo telescope, $D \approx 300$ m) can only provide a rather crude positional accuracy for pulsars (~ 2.2 arcmin full-width-half-maximum at 1.6 GHz). For the experiments outlined above to work, however, the pulsars' positions and proper motions must be known to an accuracy on the sub-milliarcsecond level. Even though pulsar timing can provide accurate solutions for these parameters, they are – especially for normal pulsars – effected by timing noise reducing the precision. Furthermore, for binary pulsars in a globular cluster relativistic parameters derived from pulsar timing (e.g. the observed orbital period decay and the Shapiro delay) are effected by the transverse motion (the "Shklovskii Effect", see Lorimer & Kramer 2005). In order to improve the timing solutions by fixing, e.g., positions and proper motions of pulsars, model independent direct astrometry of pulsars as a complementary observational approach is required. The best observational technique providing the astrometric precision needed is very long baseline interferometry (VLBI). In VLBI radio telescopes around the globe are combined to form one very large virtual radio dish whose angular resolution is inversely proportional to the largest distance in between any two telescopes that are part of the array.

In this project, we are observing the globular cluster M15 (also designated NGC 7078) in a multi-epoch VLBI campaign. M15 is one of the most metal-poor GCs with a metallicity of only 0.4 per cent of the solar value (Sneden et al. 1997). Its estimated age of 13.2 Gyr (McNamara et al. 2004) shows that it is one of the oldest Galactic globular clusters. Additionally, stellar surface density profiles of M15 reveal a steady increase towards the center of the cluster indicating a state of advanced core-collapse (e.g. Djorgovski & King 1986). As a result, stellar encounters should take place frequently favouring the formation of MSPs and X-ray binaries especially in the core region of the cluster. In fact, M15 is known to host at least eight pulsars

Table 1.1: Details of the eight known pulsars in M15 as they are published in the *ATNF Pulsar Catalogue* (`http://www.atnf.csiro.au/research/pulsar/psrcat/`, Manchester et al. 2005).

Name	RA (J2000)	DEC (J2000)	Dist [$''$] [a]	P [s]	$\dot{P}$ [ss^{-1}]
J2129+1210A	21:29:58.2	+12:10:01.2	1.53	0.110665	-2.10e-17
J2129+1210B	21:29:58.6	+12:10:00.3	4.30	0.056133	9.54e-18
J2129+1210C	21:30:01.2	+12:10:38.2	55.67	0.030529	4.99e-18
J2129+1210D	21:29:58.2	+12:09:59.7	2.08	0.004803	-1.08e-17
J2129+1210E	21:29:58.1	+12:10:08.6	7.52	0.004651	1.78e-19
J2129+1210F	21:29:57.1	+12:10:02.9	17.24	0.004027	3.20e-20
J2129+1210G	21:29:57.9	+12:09:57.3	7.21	0.037660	2.00e-18
J2129+1210H	21:29:58.1	+12:09:59.4	3.20	0.006743	2.40e-20

[a] Distance from the assumed cluster center at RA = 21:29:58:35, DEC = 12:10:01.5

and two low-mass X-ray binaries (LMXBs), one of which is also detectable as a radio source. Table 1.1 lists a few details of the known pulsars in M15 among which are the pulse period P and the pulse period derivative $\dot{P}$. Except for two pulsars all of them have rotation periods below 40 ms placing them clearly in the MSP regime. The small distance of less than 4.5 arcsec (corresponding to ~ 0.25 pc at M15's distance of 10.3 ± 0.4 kpc) from the cluster center of four of the pulsars makes those targets especially interesting for studies of cluster dynamics. The MSP J2129+1210C is known to have a binary companion which is a neutron star turning this system into a laboratory for tests of General Relativity. In addition to M15 being of major interest in terms of its pulsars and LMXBs, various authors have claimed it to host an intermediate mass black hole (IMBH, e.g. Gerssen et al. 2002, Maccarone 2004).

In total, we are observing M15 in six epochs spread over a little less than two years from November 2009 to June 2011. Our VLBI array is made up of nine antennas spreading over Europe, the USA and Puerto Rico providing a maximal angular resolution of 3.5 mas at our central observation frequency of 1.6 GHz. We have designed the experiment as to achieve a number of goals. First of all, we want to detect the already known pulsars and measure their apparent proper motion across the sky. For the pulsars closest to the core of M15 we want to use the proper motion results to determine the pulsars' orbits about the central mass and, thereby, give an estimate on the mass of the central object. If this central source really is an IMBH moving with the global motion of the globular cluster, it should be detectable in our survey exhibiting a proper motion slightly different from the one of the close-by pulsars. Furthermore, using our proper motion results we want to improve the pulsar timing model of the binary pulsar J2129+1210C for which there exist more than 20 years of timing data. Additionally, our data set is sensitive enough to potentially enable us to detect compact sources that were missed in previous surveys.

This thesis is organized as follows: In Chapter 2, I will give a brief introduction about the observational characteristics of pulsars that led to the development of theoretical models describing their emission and formation mechanisms. The theoretical background of our observational technique of choice, VLBI, will be described in Chapter 3. It includes the basics of a two-element radio interferometer, the principles of aperture synthesis (the combination of more than only two radio telescopes) and the discussion of problems that are specific to VLBI. I will describe our actual observational set-up and the data reduction procedure in Chapter 4. At the time of writing of this thesis, only four of the six observation epochs had been correlated, reduced, and analyzed. Therefore, Chapter 5 will be spent on the preliminary results we obtained while they will be discussed in Chapter 6. Concluding remarks and a short outlook of what is to come can be read in Chapter 7.

2 Pulsars

Neutron stars, usually detected as pulsars, are laboratories to test the laws of physics at extreme conditions. With radii of about 10 km and masses of approximately 1.4 solar masses ($M_\odot$) they are among the most compact objects known to exist. Franko Pacini was the first to predict that an object like a rotating neutron star could be the source of energy in the Crab Nebula (Pacini 1967) and Jocelyn Bell was the first to actually observe one in 1967 (Hewish et al. 1968). Since then, neutron stars (NSs) have become a major field of research in astronomy and they have contributed significantly to our understanding of, e.g., stellar evolution, the structure of the Milky Way and gravitational physics. In the following, I will briefly summarize observational characteristics of pulsars, their formation mechanism and their relevance for astrophysics in terms of astrometry.

2.1 Observational characteristics of pulsars

In 1967, Jocelyn Bell detected a signal with a very distinct, repetitive pattern in her 81.5 MHz observations of the northern sky. These pulses had a very stable period of about 1.337 seconds and seemed to originate from a specific location in the sky. Furthermore, they did not reveal any parallactic motion greater than 2 arcminutes and, hence, the source of the emission could only be extraterrestrial and it also had to be at a large distance from the solar system (Hewish et al. 1968). Shortly after this discovery many more such objects were detected, all of them having pulsation periods ranging between a few fractions of a second to about 10 seconds.

Today, more than 1900 pulsars are known throughout the Galaxy.[1] The vast majority of them are detectable at radio frequencies,[2] many of them have also been confirmed to be visible at optical, x-ray and even at gamma-ray wavelengths. In the radio regime, the emission is highly linearly polarized (e.g. Graham-Smith 2003) and all pulsars show a very characteristic spectral

[1] For a compilation see `http://www.atnf.csiro.au/research/pulsar/psrcat/`, (Manchester et al. 2005)

[2] As a matter of fact, recent Fermi LAT data has revealed radio-quiet pulsars detectable at high energies (γ-ray) only (Abdo et al. 2009, Saz Parkinson et al. 2010)

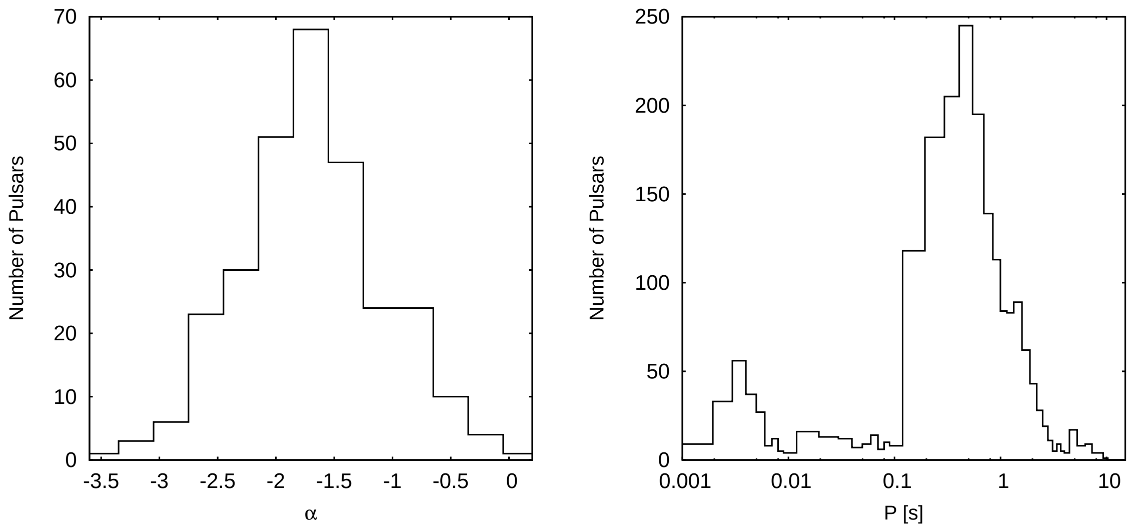

Figure 2.1: Number counts of pulsars with similar spectral index α (left) and of pulsars with similar pulsation frequency P (right). Note the bimodal distribution of pulse frequencies. Both plots were produced with the data published in the *ATNF Pulsar Catalogue*.

energy distribution S_ν following a power law

$$S_\nu \propto \nu^\alpha$$

where ν is the emission frequency and α is the spectral index. For pulsars α is negative with a mean value of $\alpha \sim -1.8$ (Maron et al. 2000, Figure 2.1 left). Thus, pulsar emission is strongest at low frequencies. Additionally, broadband radio observations of pulsars have revealed that the signal is strongly dispersed – the lower the observing frequency the more the signal lags behind that at a higher frequency. This, however, is not a property intrinsic to pulsars but instead is an effect caused by the interstellar medium (ISM): Free electrons along the line of sight to the pulsar disperse the radio signal (see section 2.3 for a further discussion).

The combination of linear polarization and a negative spectral index points to the notion that pulsar emission is non-thermal but coherent curvature radiation instead. Thus, it originates from charged particles – mostly relativistic electrons and positrons – that are being accelerated in strong magnetic fields. The extremely stable yet individually different pulsation characteristic of these signals led to the conclusion that their origin must be rapidly rotating objects, whose beams of emission only strike the observer at intervals equal to the rotation rate of the emitting sources. The fact that the emission is beam-like, meaning that it is not isotropic but directional instead, together with the aforementioned observation that it is curvature emission, points to a magnetized rotator whose rotational axis is misaligned with the magnetic field axis. Hence, the

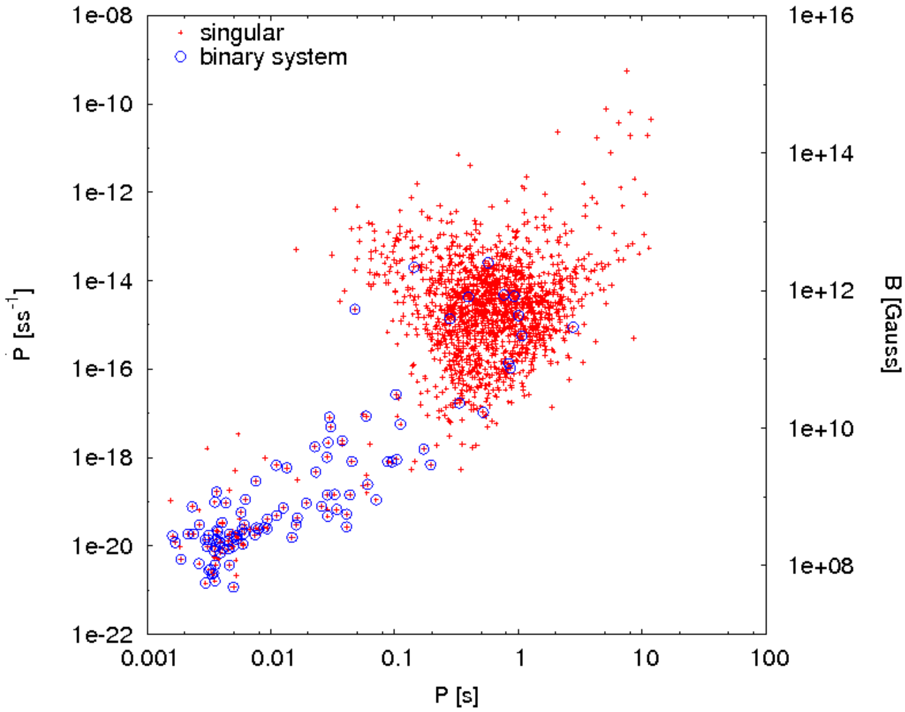

Figure 2.2: Compilation of all pulsars as published in the *ATNF Pulsar Catalogue* in May 2011. Plotted is the correlation between the pulsar frequency and both the spin down rate $\dot{P}$ and the derived magnetic field strength B at the surface of the NS. Red crosses represent solitary pulsars, blue circles indicate binary systems.

high rotation rate and the strong magnetic field needed to explain the observations, led to the conclusion that the source of the emission must be a fast spinning neutron star with a strong bipolar magnetic field – a pulsar.

When looking at the population of pulsars in a P-$\dot{P}$ diagram (Figure 2.2), where P denotes the pulsation period and $\dot{P}$ its derivative with respect to time, it becomes obvious that there are two different populations of pulsars. The majority of these objects exhibit pulsation frequencies of about one second whereas a small but significant subgroup of pulsars have periods of only a few milliseconds (further emphasized in Figure 2.1 right). Furthermore, the spin-down rates of the two groups differ by roughly five orders of magnitude – fast spinning pulsars have more stable rotation periods than slow ones. The surface magnetic field strength B of pulsars is proportional to P and $\dot{P}$:

$$B \propto \sqrt{P\dot{P}} \,.$$

Therefore, when plotting the pulsation frequency against the surface magnetic field (Figure 2.2) the exact same bimodal distribution appears. The magnetic field strength on the surface of fast spinning, so called recycled or millisecond pulsars (MSPs), are weaker by about four orders of magnitude compared to the 'normal' pulsars. The third characteristic of this bi-modality, which also provides the explanation for the observed differences in the two populations, is the fact that most MSPs are bound in a binary systems whereas the regular pulsars are mostly solitary ones.

2.2 The formation mechanism of (recycled) pulsars

Heavy stars with initial masses beyond eight solar masses ($M_\odot$) undergo all burning stages from Hydrogen to Silicon. During the nuclear fusion process ever heavier elements are build up and the mass of the newly fused core is lower than the sum of the masses of the reactants. This difference in mass is called the 'mass excess' which is released in form of electromagnetic radiation. This radiation heats and ionizes the matter surrounding the core and, hence, is the source of energy for the thermal and radiation pressure counteracting gravity. Both forces together ensure that the star remains in hydrostatic equilibrium throughout its evolution. Finally, at the end of its life time, the core of such a star is entirely made up of iron-like species which cannot supply the star with energy by going through further nuclear fusion stages. As a result, the radiation pressure ceases to counteract the gravitational force and the star collapses under its own gravity - an event which gives rise to what is known as a core collapse supernova (SN).[3]

Depending on the mass of the iron core before collapse, it will either disrupt entirely, form a black hole (BH, for core masses $M_c \gtrsim 2.5M_\odot$) or it will turn into what is know as a neutron star (NS, $1.9M_\odot \lesssim M_c \lesssim 2.5M_\odot$). In the latter case, during collapse, the matter density inside the core reaches a level exceeding that of atomic cores. As a result, electrons are captured by protons leaving nothing but an object made up of neutrons in the core region[4] and relativistic electrons and protons towards the outer layers (see Y Potekhin 2010 for a review on NSs). In such an object neutron degeneracy pressure keeps it from collapsing further into a black hole. The remaining matter formerly surrounding the core of the progenitor is blown away in a rebounce process and it is further heated and accelerated by the gravitational energy released mostly in the form of neutrinos during collapse. This material is highly excited and radio-active species heavier than iron are fused. Shortly after fusion these species (mostly ^{56}Ni and ^{56}Co) start to decay giving a core-collapse supernova light curve its characteristic shape (see, e.g., Janka et al. 2007 for a full review of SNe).

A star with an initial mass $M_i \sim 8$ - 15 $M_\odot$ will end its life in a core collapse SN leaving behind a neutron star with a typical radius $R_{\rm NS} \sim 10$ km and a mass $M_{\rm NS} \sim 1.4$ $M_\odot$. Due to angular momentum conservation this very compact object has high rotation rates and, in case the core

[3] Core collapse SNe are SNe Type Ib, Ic and Type II. Type Ia SN are the result of a nuclear fusion runaway process after which no remnant is left behind.

[4] The very core itself could be composed of exotic matter like pion condensates, lambda hyperons, delta isobars, and quark-gluon plasmas.

of the progenitor was magnetized, it will have a strong magnetic field because of magnetic flux conservation. The magnetic field is tied to the core and, thus, co-rotates with the NS. In the vicinity of the magnetic poles, charged particles (that make up the hot plasma co-rotating with the NS) are accelerated along the magnetic field lines. Following Maxwell's Equations they give rise to linearly polarized curvature radiation. Due to the high magnetic field strength and the high electron density in the plasma surrounding the NS a coherent beam of electro-magnetic radiation is formed along the magnetic field axis. If this axis is not aligned with the rotational axis of the NS the result will be a type of "lighthouse-effect": The beamed emission strikes the observer only at intervals equal to the rotational rate of this pulsar, if at all.

The progenitors of core collapse supernovae are massive stars, most likely O and B type stars, the majority of which ($\sim 70\%$) are found in binary systems (Batten 1967). Usually, the two stars have differing masses with the more massive one evolving at a higher pace. When the more massive companion collapses, possibly forming a pulsar, it is very likely that the binary is disrupted forcing the two stars to follow different trajectories from then on. Thus, it is safe to assume that most pulsars are born as solitary objects. The majority of pulsars are believed to be born with pulse periods of about 0.1 seconds or less and with very strong magnetic fields of the order of $\sim 10^{12}$ Gauss. The continuous emission of radiation reaching from the radio to the gamma ray regime, however, causes the pulsar to lose energy. Since the only source of energy for an isolated pulsar is its rotational energy it consequently slows down over time, giving rise to the observed pulse period derivative $\dot{P}$.

Even though most pulsars might be born as solitary object, we still observe a considerable number of pulsars that are bound in binary systems and that exhibit properties different from that of the non-binaries. Therefore, these pulsars either remained bound to their companion star even after the SN or, which is more likely, they were trapped in the potential well of another star they encountered on their trajectory. The highest probability for stellar captures to occur is in the central region of globular clusters (GC) where the density of stars peaks.[5] As a matter of fact, the majority of pulsars that are part of a binary system (and also MSPs) were detected in GCs, with Terzan 5 and 47 Tucanae leading the field hosting 33 (Ransom et al. 2005) and 23 (Camilo et al. 2000, Freire et al. 2003 and references therein) confirmed pulsars, respectively.

Consider a pulsar in a close orbit with a companion star. The latter – if massive enough – will eventually evolve to a giant filling its Roche lobe. As of that point the pulsar will start to accrete matter which is heated by friction such that the system is quite likely to become visible as a low mass or high mass X-ray binary (LMXB or HMXB, depending on the mass of the companion

[5] Note that a high stellar density also implies that binary systems can be dusrupted due to further stellar encounters. Therefore, the companion star of a pulsar that we observe today is not necessarily its first companion.

star). The accretion of matter by the NS leads to a decrease of its rotational period – the pulsar is spun up to become a recycled pulsar, also referred to as millisecond pulsar (see Lorimer 2008 for a review of MSPs). Obviously, it will take a considerable amount of time from the moment of birth of the original NS until it has been captured (and / or the initial companion has evolved to the giant stage in case the binary was not disrupted during the SN) and spun-up as described here. Hence, MSPs are to be expected to be older than normal pulsars. In fact, the characteristic age τ_c of pulsars given by the relation

$$\tau_c = \frac{P}{2\dot{P}}$$

differs significantly between the two populations. For normal pulsars it is in the range $\tau_c \sim 10^{6-7}$ years as compared to $\tau_c \sim 10^9$ years for MSPs. Assuming τ_c to be a measure for the real age of pulsars the observed discrepancy in pulsar spin-down rate and in magnetic field strength between fast and slow pulsars can be explained. First of all, normal pulsars continually lose rotational energy and eventually fade beyond detection as outlined above. As a result, very old slow pulsars should exist but they are simply 'switched off' – they do not radiate anymore. Hence, we do not see old regular pulsars. Secondly, old spun-up MSPs gain angular momentum through accretion and their magnetic field strength decreases during that process. The decline in magnetic field strength results in the fact that relativistic particles are not accelerated as much and, thus, the MSP loses less energy per rotation as compared to normal pulsars. Consequently, the rotation periods of MSPs are much more stable as can be seen in Figure 2.2.

2.3 Pulsar astrometry

As mentioned in section 2.1, the first detection of a pulsar happened by pure chance. Since then, many observational campaigns have been dedicated to pulsar searches improving our understanding of these objects tremendously. In addition to being laboratories to test particle physics and the equation of state of matter at super-nuclear densities, pulsars can be used, e.g., to probe the Galactic electron density distribution, they are of help at tying different frames of reference to one-another, and in the case of MSPs (especially when bound in a binary) their rotation periods are accurate enough to be used as clocks in tests of General Relativity (GR, e.g. Kramer & Wex 2009). Moreover, proper motion measurements of pulsars can be used to trace their trajectories back to their birth sites within the Galactic gravitational potential (e.g. Vlemmings et al. 2004) and in case they are members of a GC cluster dynamics can be studied.

The aforementioned dispersion of the pulsar signal is an effect known as the dispersion measure DM. Assuming the electron density n_e along the line of sight to a pulsar is known one can use the measured delay Δt between the arrival of one and the same pulse at frequencies ν_1 and ν_2

(with $\nu_1 < \nu_2$) to determine the distance d to the source:

$$\Delta t \propto \left(\frac{1}{\nu_1^2} - \frac{1}{\nu_2^2}\right) \cdot \int_0^d n_e \, dl \ .$$

In this approach, the integral over the path length dl to the pulsar is what is defined as DM and its upper bound d is shifted to match the observed time delay Δt. Of course, the Galaxy electron distribution n_e is a major parameter with high uncertainties in need of constant refinement (e.g. Cordes & Lazio 2003). On the other hand, turning the argument around, one can probe and confine the Galactic electron density model if the distance to pulsar has been measured by other means such as pulsar timing or parallax measurements.

In pulsar timing one makes use of the stable pulsation rate and the time of arrival (TOA) of individual pulses depending on Earth' position in ecliptic coordinates. Knowing the light travel time from the Sun to the Earth (τ ~8.3 minutes) and also knowing the exact location of the observer within this heliocentric coordinate frame at the time of observation the ecliptic position of the pulsar can be deduced. Assuming that at some time t_0 the observer is at the closest point to the pulsar, he or she will be at the farthest point six months later having moved by 180 degrees in ecliptic coordinates. Hence, the distance to the pulsar will have increased by 2 AU (assuming it lies within the plane of the ecliptic) and the TOA will be delayed by $\Delta t = 2AU/c$, where c is the speed of light. Assuming for simplicity a circular orbit of Earth around the Sun, the time delay Δt for a pulsar at ecliptic longitude λ and ecliptic latitude β is given by

$$\Delta t = \tau \, cos(\omega t - \lambda) cos\beta \ ,$$

where ω is the angular velocity of the Earth in its orbit. Thus, long-term observations at regular intervals over at least one year will yield a sinusoidal behaviour of the time delay as depicted in Figure 2.3. Simply speaking, correcting the pulse TOA by the equation given above it is possible to determine the position of a 1s-pulsar to an accuracy of about 0.1 arcsec (and much better for millisecond pulsars). However, there are several geometrical factors that complicate the ecliptic coordinate system somewhat: The Earth' orbit is elliptical not circular; one needs a correction to the barycenter (the center of mass of the solar system lies

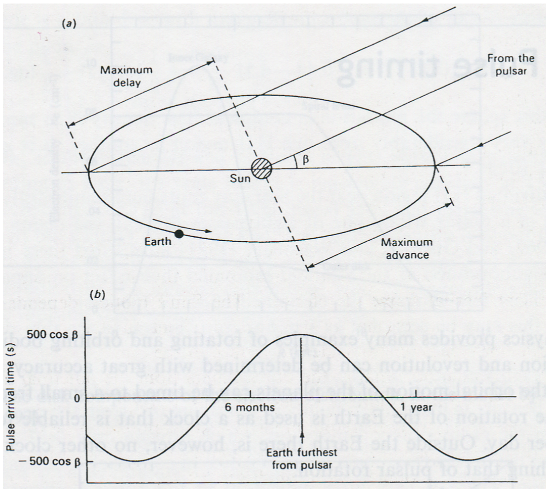

Figure 2.3: (a) The annual variation in pulse arrival time due to the Earth's orbital motion around the Sun. (b) The amplitude of the variation is 500 $cos\beta$ seconds, where β is the ecliptic latitude of the pulsar. The phase of the sinusoid is used to determine longitude. (Lyne, A.G, 1998)

just outside the Sun's surface); one needs a very accurate model of the ephemeris for which the solar system planets' masses need to be known with high accuracy; the Earth rotates adding an additional time delay of as much as one Earth radius and it gives rise to a shift in the observed frequency due to the Doppler effect. Once having modeled this geometry correctly, there are several parameters that introduce positional inaccuracies $\delta\lambda$, $\delta\beta$ that need to be taken into account. The most obvious are the parallax, the proper motion, and the spin-down rate $\dot{P}$ of the pulsar. Inherent to these parameters are the aforementioned motion of the target in the gravitational potential of a GC or in a binary system or both. Furthermore, the Sun's gravitational potential adds a time delay (the Shapiro delay) as predicted by General Relativity.

Obviously, when trying to find solutions for all parameters at once degeneracies between, e.g., the orbital motion of a pulsar in a binary system and its overall motion on the sky, are inevitable. In order to lift such degeneracies one relies on results from other methods. One such method is very long baseline interferometry. Using VLBI techniques, very accurate, model-independent solutions for parallaxes and proper motions can be determined reducing the number of free parameters in a fit to the timing solution. Additionally, pulsar positions determined with VLBI refer to the radio-defined International Celestial Reference Frame (ICRF2, Boboltz et al. 2010) whereas they are determined within the ecliptic coordinate system using pulsar timing. Hence, combining these positions it is feasible to tie one frame of reference to another. The same is true for pulsars detectable at optical wavelengths which then enable us to link ICRF2 to the optical frame of reference.

2.4 VLBI astrometry of MSPs in M15

Within the scope of this project, we use VLBI to detect and to measure the proper motion of the eight known MSPs and one LMXB that are all members of the globular cluster M15. M15 is a massive cluster at a distance of 10.3 ± 0.4 kpc. Its radial stellar density profile shows a steep cusp towards the central arcsecond possibly indicating an advanced stage of core collapse. Dynamical models based on line-of-sight velocities and proper motions infer a mass of 3400 solar masses within the central 1 arcsecond ($\sim$ 10 000 AU). The nature of this mass concentration is unknown, but it may be composed of neutron stars (Baumgardt et al. 2003) or an intermediate-mass black hole (IMBH, Gerssen et al. 2002).

Four of the eight pulsars mentioned and the LMXB are located within 4.5 arcsec ($\sim$ 0.25 pc) of the cluster center making M15 a promising target to detect high velocity transverse motion. The sensitivity of our data would also allow us to detect possible radio emission from the proposed central IMBH. Expecting this object to be moving along with the average motion of the entire GC, we should be able to tell it apart from other compact radio sources exhibiting high velocities relative to this source. Thus, we will be able to add evidence to the existence of an IMBH as the central mass concentration of M15.

Based on total cluster flux densities at 1.5 GHz, Sun et al. 2002 estimate that M15 could host up to about 300 pulsars. Therefore, we can expect to find compact radio sources that were missed by previous FFT-based pulsar searches because of tight orbits, eclipses or shrouding by dense clouds caused by the stellar wind of the companion star. Using proper motion measurements for all the known – and potentially new detected – members of M15 we will be able to determine their orbits about the central mass concentration and we will be able to give an estimate on the central mass itself. In addition, one of the known pulsars, the recycled pulsar J2129+1209C is in a binary system with another neutron star. For this system, there is pulsar timing data spanning a time range of more than 20 years. Using this data in conjunction with our proper motion results, it will be possible to determine the acceleration of the system within the potential well of M15 and to test GR.

3 Very Long Baseline Interferometry

Radio interferometry - the combination of at least two radio telescopes - is a technique that was first employed in astronomy in 1946 (Ryle & Vonberg 1946). The goal of this mode of observation is to achieve higher angular resolution compared to what is feasible with a single dish. The idea is a simple one: The telescopes involved mimic one big dish with a diameter that corresponds to the largest separation of any two of the telescopes forming the array. In very long baseline interferometry, the distance between radio telescopes (the baselines), if ground based, can reach up to one Earth diameter and even more if satellites in space (Space-VLBI) are involved. In this way, VLBI-observations provide the highest angular resolution – on the sub-milliarcseconds level – achievable today. Pulsar proper motions are mostly of the order of a few milliarcseconds per year and, thus, are measurable with multi-epoch VLBI campaigns. In the following chapter I will describe the principles of radio interferometry and I will elaborate on the challenges that are involved in VLBI-observation and how to tackle them.

3.1 Essentials on radio interferometry

Nowadays, radio interferometric observations are performed with large arrays consisting of many more than only two telescopes. However, the principle observables that we obtain from such measurements are the responses of pairs of antennas only.[1] Thus, in order to understand an interferometer it suffices to consider a basic two-element aperture as depicted in Figure 3.1. The two telescopes are separated by a distance $\boldsymbol{b}$ and observe a distant source in the direction of the unit vector $\boldsymbol{s}$. The statement that it is a distant source means that we consider the far-field regime in which the arriving electro-magnetic waves can be approximated as plane waves. Hence, the time of arrival of a wave front at one antenna lags behind that at the other antenna by the geometric time delay τ_g because of a simple difference in path length

$$\tau_g = \frac{\boldsymbol{b} \cdot \boldsymbol{s}}{c} , \tag{3.1}$$

[1] There are many different ways to derive the behaviour of such an interferometer. I will mainly follow Thompson 1999 and the lecture notes written by Prof. U. Klein.

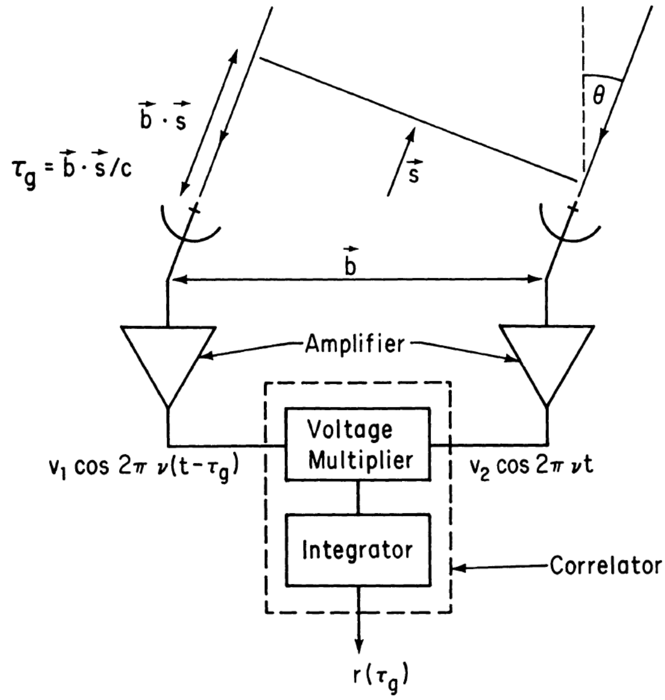

Figure 3.1: Schematic diagram of a two-element interferometer. Figure adopted from Thompson 1999.

where c is the speed of light. The responses of the individual antennas to the signal are sinusoidal voltages $V_1(t) = V_1 \cos 2\pi\nu(t-\tau_g)$ and $V_2(t) = V_2 \cos 2\pi\nu t$, respectively. The combination of the two signals is performed via cross-correlation which is defined as the time average of the product of the two signals. The output power $r(\tau_g)$ of this correlator is thus

$$\begin{aligned} r(\tau_g) &= \langle V_1(t) V_2(t) \rangle \\ &= V_1 V_2 \cos 2\pi\nu\tau_g \,. \end{aligned} \tag{3.2}$$

The product of the two voltage amplitudes V_1 and V_2 corresponds to the total received power from the observed target which, in turn, is proportional to the effective collecting area of the telescopes $A(\boldsymbol{s})$,[2] the specific surface brightness $I(\boldsymbol{s})$, and to the bandwidth $\Delta\nu$ of the receiver system. Furthermore, the cross-correlated power is sensitive to the angular extent of the target and, thus, we need to integrate over the solid angle $d\Omega$ subtended by the source S. Therefore, equation (3.2) now reads

$$r = \Delta\nu \int_S A(\boldsymbol{s}) I(\boldsymbol{s}) \cos \frac{2\pi\nu \boldsymbol{b}\cdot\boldsymbol{s}}{c} d\Omega \,, \tag{3.3}$$

where we have inserted equation (3.1) to emphasize the dependence on telescope separation

[2] Here we assume that both telescopes are alike. In case they are dissimilar the effective area is given as $\sqrt{A_1(\boldsymbol{s})A_2(\boldsymbol{s})}$

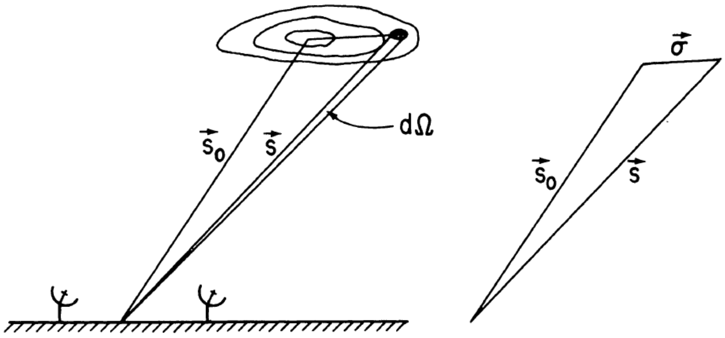

Figure 3.2: Sketch of the geometric setup between the phase reference center $\boldsymbol{s}_0$ and the response of a source within the FOV. Figure adopted from Thompson 1999.

and source direction. In all interferometric observations one defines the so-called phase tracking center for which the geometric time delay τ_g is compensated for by an instrumental time delay τ_i for reasons to be explained in Section 3.3. This phase tracking center (Figure 3.2) lies in the direction of the unit vector $\boldsymbol{s}_0$ such that

$$\boldsymbol{s} = \boldsymbol{s}_0 + \boldsymbol{\sigma} \,. \tag{3.4}$$

Rewriting equation (3.3) with this new formulation of vectors and using the trigonometric relation $\cos(\alpha+\beta) = \cos\alpha \cdot \cos\beta - \sin\alpha \cdot \sin\beta$ we arrive at

$$\begin{aligned} r = \Delta\nu \cos\left(\frac{2\pi\nu \boldsymbol{b}\cdot\boldsymbol{s}_0}{c}\right) \cdot \int_S A(\boldsymbol{\sigma}) I(\boldsymbol{\sigma}) \cos\frac{2\pi\nu\boldsymbol{b}\cdot\boldsymbol{\sigma}}{c} d\Omega \\ - \Delta\nu \sin\left(\frac{2\pi\nu \boldsymbol{b}\cdot\boldsymbol{s}_0}{c}\right) \cdot \int_S A(\boldsymbol{\sigma}) I(\boldsymbol{\sigma}) \sin\frac{2\pi\nu\boldsymbol{b}\cdot\boldsymbol{\sigma}}{c} d\Omega \,. \end{aligned} \tag{3.5}$$

At this point we can define a new complex function called the complex visibility function V which reads

$$V = |V| \cdot e^{i\phi_v} = \int_S A_r(\boldsymbol{\sigma}) I(\boldsymbol{\sigma}) e^{-i2\pi\nu\boldsymbol{b}\cdot\boldsymbol{\sigma}/c} d\Omega \tag{3.6}$$

where we have scaled the antenna response by its value, A_0, when the source position falls directly into the beam center of the antenna: $A_r(\boldsymbol{\sigma}) = A(\boldsymbol{\sigma})/A_0$. Taking a closer look at equation (3.6) it becomes obvious, that the visibility V and the source brightness distribution are closely related. Hence, measuring the visibility function we should be able to recover the intensity distribution of the source. In order to obtain a relation between the visibility and the power output of the correlator we first separate real and imaginary part of equation (3.6) and insert this into equation (3.5)

$$Re(V) = |V|\cos\phi_v = \int_S A_r(\boldsymbol{\sigma})I(\boldsymbol{\sigma})\cos\left(\frac{2\pi\nu\boldsymbol{b}\cdot\boldsymbol{\sigma}}{c}\right)d\Omega$$
$$Im(V) = |V|\sin\phi_v = -\int_S A_r(\boldsymbol{\sigma})I(\boldsymbol{\sigma})\sin\left(\frac{2\pi\nu\boldsymbol{b}\cdot\boldsymbol{\sigma}}{c}\right)d\Omega \qquad (3.7)$$

thus

$$r = A_0|V|\Delta\nu\cos\left(\frac{2\pi\nu\boldsymbol{b}\cdot\boldsymbol{s}_0}{c} - \phi_v\right) . \qquad (3.8)$$

With this formulation of the correlator output we are measuring the amplitude of the visibility function via the amplitudes of the fringe pattern cast onto the target by the interferometer. The fringe phase we measure is equal to the visibility phase ϕ_v and is measured relative to a hypothetical source at $\boldsymbol{s}_0$. Thus, the visibility phase carries the information about the position of an object relative to the phase tracking center for which $\phi_v = 0$.[3]

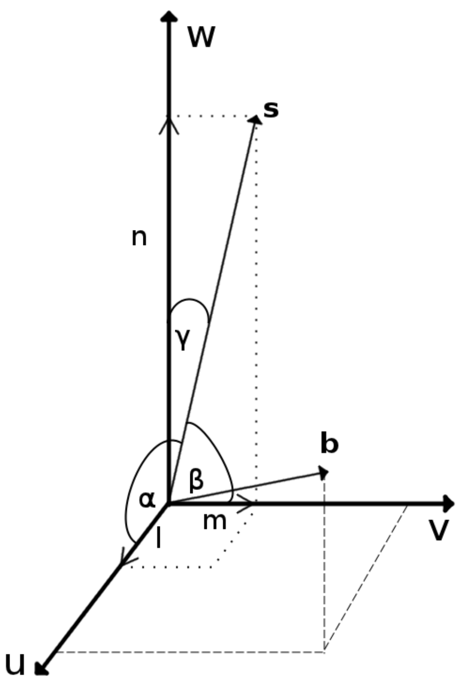

Figure 3.3: The definition of coordinates in interferometric observations.

In order to be able to apply equation (3.6) to recover the intensity distribution we need to introduce a suitable coordinate system. The system of choice are the so-called (u,v,w)-coordinates as defined in Figure 3.3. The telescopes lie in the (u,v)-plane, where u points towards east and v points towards the north. The third orthogonal coordinate w points towards the direction of interest, namely towards the phase tracking center $\boldsymbol{s}_0$. In this way, the unit vector $\boldsymbol{s}$ can be described by the direction cosines such that

$$\boldsymbol{s} = (\cos\alpha, \cos\beta, \cos\gamma) = (l, m, \sqrt{1-l^2-m^2}) , \qquad (3.9)$$

the baseline vector $\boldsymbol{b}$ has components (measured in wavelength)

$$\boldsymbol{b} = (\lambda u, \lambda v, \lambda w) \qquad (3.10)$$

and the solid angle now reads

$$d\Omega = \frac{dl\,dm}{\sqrt{1-l^2-m^2}} . \qquad (3.11)$$

[3] This is already obvious in equation (3.6) since for $\boldsymbol{\sigma} = 0$ the phase $\phi_v = 0$.

Inserting these coordinates into equation (3.6) we obtain the visibility function in terms of the (u,v,w) coordinates

$$V = \int_{-\infty}^{\infty}\int_{-\infty}^{\infty} A_r(l,m) I(l,m) e^{(-2\pi i[ul+vm+w(\sqrt{1-l^2-m^2}-1)])} \frac{dldm}{\sqrt{1-l^2-m^2}} \ . \tag{3.12}$$

As already indicated in Figure 3.3, the phase tracking center $\boldsymbol{s}_0$ is set such that the source of interest is at a small angular distance in which case $|l|, |m| \ll 1$. In this approximation[4] we arrive at the formulation of the visibility function which is but the 2-dimensional Fourier transform of the intensity distribution of the source

$$V(u,v) = \int_{-\infty}^{\infty} I(l,m) e^{-2\pi i(ul+vm)} dldm \ , \tag{3.13}$$

where we have assumed that the phase tracking center coincides with the pointing center such that $A_r(0,0) \approx 1$. Therefore, if we gather enough information about the visibility function we should be able to reconstruct the source brightness distribution by simple Fourier inversion. This, however, is an unfeasible task for one pair of antennas because such a system delivers only one data point during one integration time. Consequently, in order to sample the visibility function sufficiently, a larger number of baselines and long observations are needed, complicating the matter in that sense, that many different, constantly changing geometric time delays τ_g and also differing baseline components need to be computed.

3.2 Phased arrays and image reconstruction

The number of available baselines of an interferometer is given as $N(N-1)/2$, where N is the number of telescopes forming the array. To relate the relative distances (L_x, L_y, L_z) between individual antennas to the (u,v,w)-coordinates it is convenient to define their position in a Cartesian coordinate system whose axes point towards the direction of the meridian at the celestial equator (x-axis), towards the East (y-axis), and towards the celestial North pole (z-axis). It can be shown (Thompson et al. 1986) that the (u,v,w)-components of the baseline vectors in terms of their relative distances and the phase tracking center at hour angle h_0 and declination δ_0 are given as

$$\begin{pmatrix} u \\ v \\ w \end{pmatrix} = \frac{1}{\lambda} \begin{pmatrix} \sin h_0 & \cos h_0 & 0 \\ -\sin\delta_0 \cos h_0 & \sin\delta_0 \cos h_0 & \cos\delta_0 \\ \cos\delta_0 \cos h_0 & -\cos\delta_0 \sin h_0 & \sin\delta_0 \end{pmatrix} \begin{pmatrix} L_x \\ L_y \\ L_z \end{pmatrix} \ . \tag{3.14}$$

4 Note that with this approximation a phase error is introduced. See, e.g., Thompson 1999 for a full discussion.

If we eliminate h_0 from this set of equations we arrive at the ellipse equation describing the path one baseline maps out in the (u,v)-plane while the earth rotates

$$u^2 + \left(\frac{v-(L_z/\lambda)\cos\delta_0}{\sin\delta_0}\right)^2 = \frac{L_x^2+L_y^2}{\lambda^2}\,. \tag{3.15}$$

Since the intensity distribution of an astronomical source is a real quantity the visibility function must be hermitian: $V(u,v) = V^*(-u,-v)$. Thus, during each integration time one baseline provides two visibility data points in the (u,v)-plane, and, accordingly, maps out two elliptical paths during long observations (Figure 3.4).

The combination of numerous telescopes at different locations and varying relative distances ensures a reasonably fast filling of the (u,v)-plane and, therefore, aims at sampling the visibility function sufficiently to reconstruct the intensity distribution of the observed target. In this context it is important to note that in order to obtain a complete view of the intensity distribution it is absolutely necessary to include both long and short baselines. As mentioned earlier, a pair of antennas can be thought of as one telescope with a diameter D corresponding to the separation in between them. As a result, the synthesized beam of this system has a field of view (FOV, also called half power beam width, HPBW) $\theta \propto \lambda/D$. Therefore, each baseline is only sensitive to radiation within this angular diameter and structure beyond that is said to be resolved out. Hence, long baselines do not detect extended emission which is why shorter baselines are essential to obtain information about the entire flux of a source. The FOV of an interferometer as such is defined by the largest antenna that is part of the array. The reason is simple, since the only signals that can be correlated are those that are at a distance σ from the phase tracking center $\boldsymbol{s}_0$ (which mostly coincides with the pointing center of each antenna) that is within the FOV of all other antennas as well.

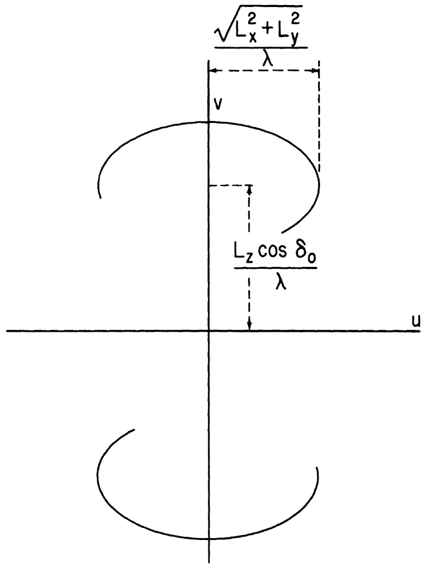

Figure 3.4: Elliptical projection of one baseline vector onto the (u,v)-plane while a source is tracked across the sky. The two trajectories are complex conjugates of one-another. Figure adopted from Thompson 1999.

Nevertheless, no matter how densely spaced the visibilities are measured – and in most cases the sampling is not dense at all – we will never obtain a continuous but only a discrete set of data points. Therefore, inverting equation (3.13) and replacing the integral by a sum the formulation for the intensity distribution as measured with the interferometer takes the form

$$I^D(l_s, m_s) = K \cdot \sum_{k=0}^{2n} V(u,v) \cdot S(u,v) \cdot e^{2\pi i(u_k l_s + v_k m_s)} \ . \tag{3.16}$$

In this formulation, the pre-factor $K = (2n+1)^{-1}$ ensures normalization of the sum which is computed for all $2n$ visibilities. The weighted sampling function

$$S(u,v) = \sum_{k=0}^{2n} W_k \delta^2(u - u_k, v - v_k) \tag{3.17}$$

takes care of the discretization of the data. The weighting factor W_k can be chosen to emphasize certain visibilities more than others and, thus, manipulates the beam shape of the array. The two extremes of natural and uniform weights ensure best signal-to-noise and best angular resolution, respectively. This is done by assigning the same weights either to each visibility (natural) or each location in the (u,v)-plane (uniform).

The intensity distribution given in (3.16) is called the *dirty image* since it is a convolution of the actual intensity distribution $I(l,m)$ with the point spread function of the interferometer, also called the dirty beam $B(l,m)$

$$B(l_s, m_s) = \sum_{k=0}^{2n} S(u,v) e^{2\pi i(u_k l_s + v_k m_s)} \ . \tag{3.18}$$

Thus, to recover the sky image, $I(l,m)$, we need to perform a deconvolution which is mostly done using the CLEAN algorithm (Högbom 1974) and variants thereof. Before running CLEAN, the dirty image and the dirty beam are computed either by the direct Fourier transform which means evaluating the sums in (3.16) and (3.18) or by applying a fast Fourier transform algorithm that involves interpolating the data onto a rectangular grid (see Briggs et al. 1999 for details). The CLEAN algorithm starts off by searching for an intensity peak in the dirty image. Next, the dirty beam is multiplied by the scaled strength (a factor of 0.1-0.2 is common) of the intensity peak and is then subtracted from the dirty image at the position of the detected peak. The scaled peak and its position are recorded in a model in form of δ-function. The search for remaining peaks is continued until a user-defined level for the strength of a peak to be considered as such is reached. Alternatively, the loop stops as soon as a defined number of model components (peaks in the dirty image) is exceeded. From then on, the algorithm continues by smoothing the model composed of δ-function with the CLEAN beam which is usually an elliptical Gaussian (best approximation of the main lobe). As a last step, the residuals of the dirty image are added, giving information about the noise of the map.
With this method strong side lobes as depicted in the left panel of Figure 3.5 can be removed

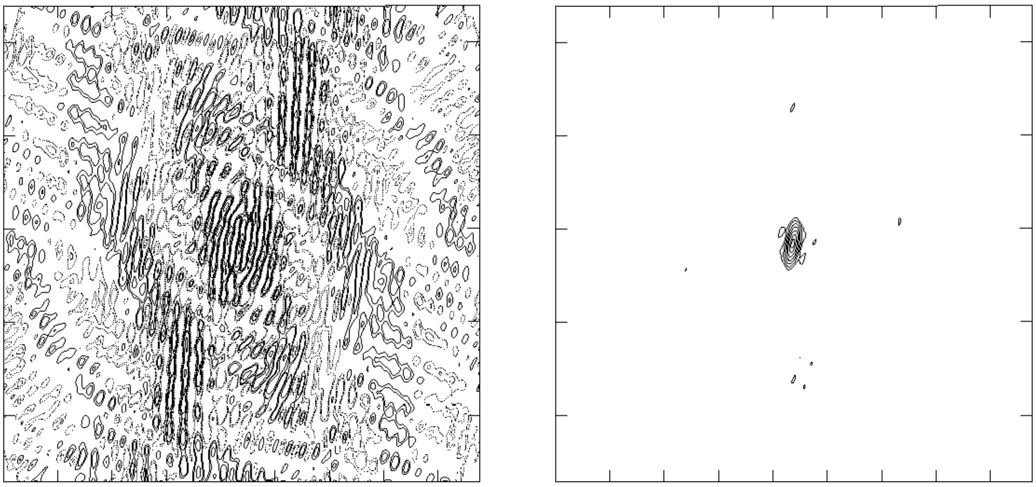

Figure 3.5: The effect of deconvolution performed on the phase calibrator J2139+1423. Left: The dirty image before running CLEAN. Right: The CLEAN image after deconvolution with CLEAN. Contours are (-5, -3, 3, 5, 10, 20, 40, 80, 120) times the rms value (7 mJy) of the CLEAN image. The elongation in North-South direction is due to unequal uv-coverage.

to recover the flux and structure of the target. Note that the elongation of the recovered point source in Figure 3.5 right is due to shorter baselines in the North-South direction.

3.3 Effects of bandwidth and integration time

In the derivation of the correlator output (equation (3.8)), we have thus far ignored the effect of a finite bandwidth that is introduced by the explicit dependence on the frequency of the cosine term. Effectively, the fringe amplitude at a given visibility phase ϕ_v will be different at each frequency across the bandwidth. Accounting for this fact, we rewrite (3.8) as a differential

$$dr = A_0|V|\cos(2\pi\nu\tau_g - \phi_v)\,d\nu \,, \tag{3.19}$$

which after integration over a rectangular bandpass with a central frequency ν_0 yields for the cross-correlated power

$$r = \mathrm{sinc}(\Delta\nu\tau_g)A_0|V|\Delta\nu\cos(2\pi\nu_0\tau_g - \phi_v) \,, \tag{3.20}$$

Thus, because of the finite bandwidth an attenuation factor (also known as the delay beam) is introduced dampening the fringe amplitude considerably for $\Delta\nu\tau_g > 1$ (Figure 3.6). For sensitivity reasons reducing the bandwidth is unfavourable and, hence, the geometric time delay needs be compensated for by an artificial instrumental time delay τ_i. This delay is introduced at the antenna where the wave front arrives first just before the correlation of the signal. The argument of the sinc-function in (3.20) is therefore replaced by $\Delta\nu(\tau_g - \tau_i)$. Usually, the instrumental time delay τ_i is computed such that the pointing centers of the antennas of the array and the phase tracking center coincide since this is where the antenna beam is most sensitive. However, this is not a necessity and the delay beam of the array can be manipulated to point somewhere different than the antennas.

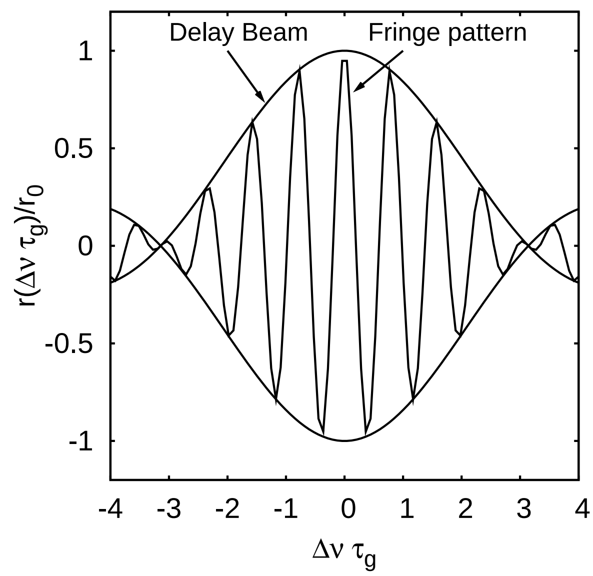

Figure 3.6: Output of the correlator scaled by its maximum value r_0 when $\Delta\nu\tau_g = 0$. The larger the chosen bandwidth the narrower the delay beam will be.

A further complication induced by the bandwidth is known as bandwidth smearing. At any given time we measure the visibility function not only at the central observing frequency ν_0 but also at adjacent frequencies. Consider two adjacent frequencies ν_1 and ν_2 with wavelengths λ_1 and λ_2 in equation (3.15). Obviously, if the visibilities at both wavelengths are measured separately, they will map out two close-by paths in Figure 3.3. However, since both frequencies are measured as one visibility they will, in fact, not map out an ellipse but rather an elliptical area in the (u,v)-plane. Thus, if not accounted for, the bandwidth will result in a radial smearing of the visibility (Figure 3.7 left) with an angular extent β that can be shown (Thompson 1999) to be

$$\beta \approx \frac{\Delta\nu}{\nu_0}\sqrt{l_1^2 + m_1^2}\,.$$

Similarly, the integration time τ_a leads to an averaging of visibilities in the (u,v)-plane that effects the intensity distribution of a source in the image domain. Namely, during each integration time the projection of the baseline components onto the (u,v)-plane will change by an angular amount $\omega_e\tau_a$, with ω_e being the angular velocity of Earth. Therefore, we do not measure individual points along the elliptical path but small lines instead (Figure 3.7 right). The extent of the smearing is once again proportional to the distance $d = \sqrt{l^2 + m^2}$ from the phase tracking center.

Both bandwidth and time smearing need to be taken into account when doing wide field imaging as is done in this project. The way to counteract these effects degrading sensitivity and angular resolution towards larger distances from the phase tracking center is by splitting the bandwidth into as many different channels as possible and by decreasing the integration time to as short an

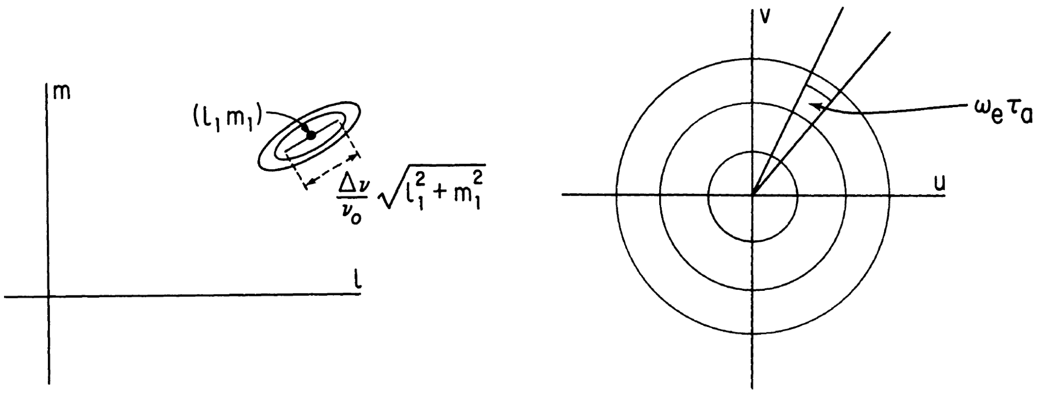

Figure 3.7: Effects of bandwidth $\Delta\nu$ (left panel) and integration time τ_a (right panel) on visibilities and thus the intensity distribution of an observed source. The bandwidth results in a radial smearing of the data in the (l,m)-plane while the time smearing is visible as circumferential smearing in the (u,v)-plane and, thus, can be thought of as a rotation in the (l,m)-plane. Both effects result in a decrease in angular resolution and in sensitivity at larger distances $|(l,m)|$ from the phase tracking center since both amplitude and phase are smeared out. Figures adapted from Thompson 1999.

interval as feasible.

3.4 Challenges in VLBI

In connected interferometers like the Very Large Array (VLA) or the Westerbork telescope the correlation of the signal is done during the observations and the computation of the geometric time delay between antennas is rather straight forward. The fringe amplitude and phase can be monitored in real time such that inaccuracies in τ_i or in the local oscillator (LO) frequency and phase can be compensated for immediately. Such rather compact arrays are insensitive to geographic subtleties effecting VLBI observations. In VLBI campaigns, owed to the large distances between telescopes, the observations at each station are first recorded on site and are then sent to a correlation facility[5] for processing. The geometric time delays are clearly very different between all stations and, furthermore, they are changing at different rates during an observation campaign lasting for, e.g., six hours. Additionally, Doppler shifts are introduced because all antennas in the array move at varying velocities relative to the source. Consequently, a very accurate geometric model incorporating factors like antenna positions, Earth rotation and ocean loading (See Table 3.1 for a complete list of geometric factors introducing path length differences and their rates of change with time.) is of vital importance for a successful removal of the attenuation caused by the geometric time delay.

[5] such as the Joint Center for VLBI in Europe (JIVE)

Table 3.1: Terms of a VLBI Geometric Model. Table adapted from Thompson 1999.

Item	Approx max Magnitude	Time scale
Zero order geometry.	6000 km	1 day
Nutation	$\sim 20''$	< 18.6 yr
Precession	$\sim$ 0.5 arcmin/yr	years
Annual aberration	$20''$	1 year
Retarded baseline	20 m	1 day
Gravitational delay	4 mas @ 90° from sun	1 year
Tectonic motion	10 cm/yr	years
Solid Earth Tide	50 cm	12 hr
Pole Tide	2 cm	$\sim$1 yr
Ocean Loading	2 cm	12 hr
Atmospheric Loading	2 cm	weeks
Post-glacial Rebound	several mm/yr	years
Polar motion	$0.5''$	$\sim$ 1.2 years
UT1 (Earth rotation)	Random at several mas	Various
Ionosphere	$\sim$ 2 m at 2 GHz	seconds to years
Dry Troposphere	2.3 m at zenith	hours to days
Wet Troposphere	0 – 30 cm at zenith	seconds to seasonal
Antenna structure	<10 m. 1cm thermal	—
Parallactic angle	0.5 turn	hours
Station clocks	few microsec	hours
Source structure	5 cm	years

In order to be able to apply the geometric model, however, each station's recorded data needs to be equipped with accurate time stamps that are synchronized in between all array components. Despite the precision of atomic clocks, offsets between the individual telescopes and instabilities on the microsecond-level are inevitable. Furthermore, as in all radio astronomical surveys, the observing frequency is down-converted with the LO to an intermediate frequency before data storage. In VLBI down-conversion is done to baseband, meaning that the lower end of the bandpass is at DC-voltage. In this process, frequency and phase instabilities of the individual LOs and the dissimilar technical equipment at the specific stations introduce further inaccuracies in the data. All these complications, however, are predictable up to a certain level and can be incorporated into the model of the correlator. The main contribution to the error of the modeled time delay, however, is given by the completely uncorrelated atmosphere above the different telescopes. The wet troposphere and especially the ionosphere add an extra time delay of up to 60 ns at 1.4 GHz which corresponds to roughly 100 cycles. Additionally, both components are variable on timescales of seconds to years which makes them unpredictable and hard to compute.

The correct computation of τ_g at all frequencies across the band and for all stations is utterly impossible. Hence, a residual delay error $\delta\tau = \tau_g - \tau_i$ will always remain giving rise to a residual fringe phase. These errors change with time resulting in the so-called fringe rate and they are different across the band showing up as a phase slope. The best way to improve the amplitude and phase information after correlation is done via phase referencing.

This process involves the observation of a strong calibrator source that is close (within $\sim 5°$) to the target. Ideally, it should be a point source of very accurately known position not exhibiting any structure even for the longest baselines of the array.[6] The observations of the target need to be interrupted for regular scans of the calibrator to account for the time dependence of the delay errors. The main principle of phase referencing is that a point source at the position of the phase tracking center has by definition zero phase. This is true for all frequencies across the bandpass and for all times of the observations. Thus, any phase offsets, phase slopes or rates in the correlated data have to be due to an imperfect model and can be eliminated. The solutions found in this way can then be applied to the data of the observed target for calibration.

In this way, the most striking delay errors can be removed but a residual phase error will still remain. This residual error arises from the fact that even though the calibrator is close to the target the atmosphere along both lines of sight is still slightly different. Furthermore, short-term variability of the ionosphere that effects individual scans of the target cannot be accounted for by this method. Therefore, it is useful to have a strong point source within the field of view that can be used for self-calibration. The underlying principle is that we assume a model for the intensity distribution of the source and adjust the measured visibilities such that after Fourier inversion and deconvolution the model and the reconstructed image agree as much as possible.

[6] A list of suitable calibrators can be found on the VLBA web page: `http://www.vlba.nrao.edu/astro/calib/`

4 Observations and Data Reduction

The four observations included in this analysis were conducted on 11 November 2009, 7 March 2010, 5 June 2010, and 2 November 2010. The array chosen for the campaign consists of a total of nine telescopes that are spread over Europe, Puerto Rico and the USA. Namely they are the telescopes at Jodrell Bank (Jb, England), Onsala (On, Sweden), Westerbork (Wb, The Netherlands), Effelsberg (Ef, Germany), Noto and Medicina (Nt and Mc, Italy), Toruń (Tr, Poland), Arecibo (Ar, Puerto Rico), and the Green Bank Telescope (Gb, USA). The raw data is recorded at the individual stations and then sent off to Dwingeloo, the Netherlands, to be correlated at the EVN-MkIV correlator (Schilizzi et al. 2001) at the *Joint Institute for VLBI in Europe* (JIVE). The successfully correlated data can then be downloaded from the *EVN Data Archive at JIVE*.[1]

4.1 Observational setup and strategy

The choice of telescopes and of the central observing frequency of 1.6 GHz was driven by the need for high angular resolution and high sensitivity at the same time. The array configuration described above allows for both requirements to be met. First of all, we ensure a good coverage of the uv-plane (Figure 4.1 left) by combining short baselines of approximately 266 km (Effelsberg-Westerbork) with very long ones reaching more than 7500 km (e.g. Noto-Arecibo). Furthermore, the inclusion of telescopes such as Onsala and Noto provides long North-South baselines ($\sim$ 2000 km) needed to reach high angular resolution in declination (high resolution in right ascension is achieved much more easily since East-West baselines are numerous and can reach up to one Earth diameter in length; see Table 4.3 for the achieved angular resolution in each epoch.). The largest dishes of the array – Arecibo (300 m), Effelsberg (100 m) and the GBT ($\sim$ 100 m collecting area) – ensure for the high sensitivity needed to detect the faint pulsar signals. By conducting the observations at L-band (1.66 GHz central observing frequency) we make a good compromise between astrometric precision and detectability of pulsars: A higher frequency would result in an improved angular resolution but the steep spectrum of pulsars would render them undetectable. On the other hand, the pulsars would be more easy to detect at a lower frequency but only for the price of insufficient astrometric precision.

[1] http://archive.jive.nl/scripts/listarch.php

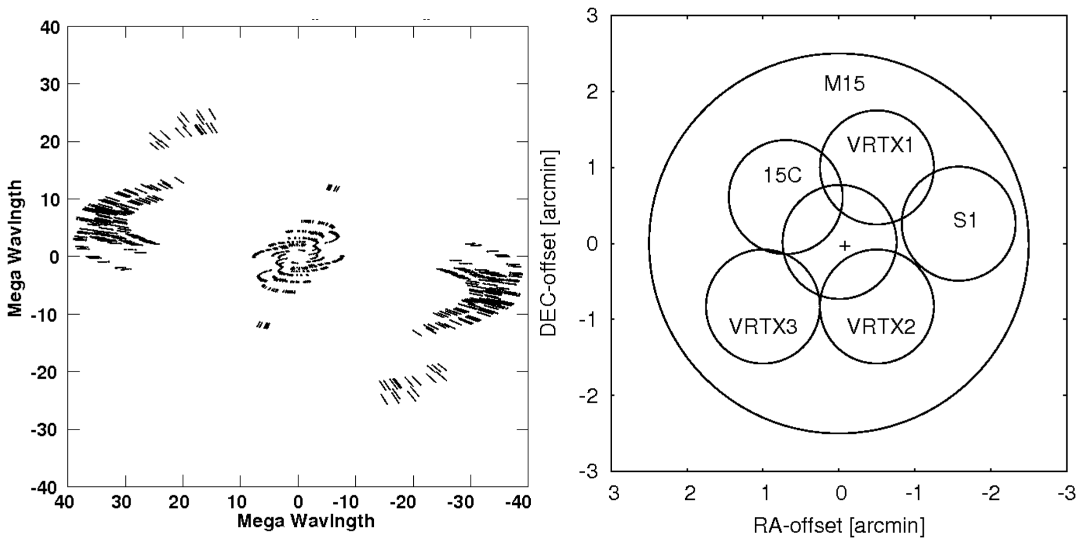

Figure 4.1: Left: UV-plane coverage achieved in epoch 3. Right: Sketch of the FOV (large circle) and the positions of the six correlation centers relative to the pointing center (indicated by the cross at (0,0)). The central circle with no label corresponds to the correlation center labeled AC211 in Table 4.2. Note that the FOV is constrained by the Arecibo beam and that the radius of the six correlation centers is defined as to allow a maximal loss of 10% in the response of a point source caused by time and bandwidth smearing.

As explained in chapter 3.2, an interferometer can be considered as a single dish having a diameter corresponding to the longest baselines involved. On the other hand, the field-of-view (FOV) of an interferometer is determined by the largest dish that is part of the array. In our survey, the Westerbork array – if phased up – would be the largest dish with a diameter of 2.7 km restricting our FOV to $\sim$ 14 arcsec full-width-half-maximum (FWHM). Given the angular extent of M15 at the sky ($\sim 1'$ half-light radius, Gerssen et al. 2002) we would need multiple pointings to map out the entire cluster. Therefore, we decided to use only one Westerbork antenna.[2] Consequently, the FOV of the array is constrained by the Arecibo beam ($\sim 2.5'$ FWHM at 1.6 GHz) being the largest dish in this antenna configuration. The FOV is thus large enough to map out the entire central region of M15 in only one pointing. Additionally, the FOV also comprises the strong unclassified source S1 (Johnston et al. 1991) located about $94''$ to the west of the cluster center. At this angular distance from the pointing center it is of great use as in beam calibrator. In order to counteract time and bandwidth smearing degrading our sensitivity and astrometric precision towards the outer regions of the FOV, we initially required an integration time of 0.25 seconds and a spectral resolution of 512 channels in each of the two polarizations and eight sub-bands of 16 MHz bandwidth. Accounting for the different receiver systems at the individual telescopes (Table 4.1) our total bandwidth amounts to 230 MHz on average. The size of the resulting correlated dataset in the first epoch ($\sim$ 250 GB), however, proved to be unpractical for data reduction and calibration. Therefore, observations conducted

[2] We could also have used only the innermost two dishes but would not have gained in sensitivity in doing so.

Table 4.1: Bandwidth available at the individual telescopes

	Ef	Jb	Nt	Mc	Tr	Ar	Wb	On	Gb
Bandwidth [MHz]	231	225	215	160	256	256	245	245	256

Table 4.2: Correlation centers throughout M15 used in all observation epochs after epoch one. The pointing center M15 which was also the correlation center in epoch 1 and, for completeness, the pointing centers for the bandpass and phase calibrators are provided as well.

Correlation center	RA (2000.0)	DEC (2000.0)
M15 (epoch 1 only)	21:29:58.3500	12:10:01.500
AC211	21:29:58.3120	12:10:02.679
15C	21:30:01.2034	12:10:38.160
S1	21:29:51.9025	12:10:17.132
VRTX1	21:29:56.3050	12:11:01.500
VRTX2	21:29:56.3050	12:09:11.500
VRTX3	21:30:02.4410	12:09:11.500
J2139+1423	21:39:01.3093	14:23:35.992
3C454.3	22:53:57.7479	16:08:53.561

after epoch 1 are still performed using only one pointing center but the data are correlated at six different correlations centers throughout M15 (Table 4.2). As a result, the integration time and spectral resolution could be reduced to 0.5 seconds and 128 channels, respectively. This configuration yields six different, overlapping tiles that are insensitive[3] to time and bandwidth smearing within $\sim 0.75'$ of the individual correlation centers (Figure 4.1 right). The size of each of the six sets amounts to roughly 30 GB making post-processing a lot easier. The observing schedule encompasses six hours in total and is set up such, that the target cluster M15 and the phase reference source (the quasar J2139+1423, located 3.13 degrees away from the pointing center) are observed in an alternating fashion: After each 3.5 minute scan of M15 we observe J2139+1423 for roughly 1.2 minutes. The bandpass calibrator (the blazar 3C454.3) is observed twice for about 10 minutes during each observational epoch, once at the beginning and once towards the end. Altogether, the total integration time on M15 amounts to about 3.6 hours in all four epochs. Obviously, the static setup of the Arecibo dish makes it impossible to include this antenna over the entire time range. Nevertheless, Arecibo-data is available for 85 (56) minutes of the total 3.6 hours in epoch 1 (epoch 3). Unfortunately, during epoch 2 and epoch 4 technical problems occurred at Arecibo. As a result Arecibo delivered no or unusable data. Therefore, the sensitivity and astrometric precision of these two datasets is much lower compared to the

[3] Up to a 10% loss in the response of a point source.

Table 4.3: Setup details for epoch 1 to epoch 4. Note the increase in noise level and degradation in astrometric precision for epochs 2 and 4 when Arecibo delivered no usable data. The differences in bandwidth between the epochs is attributed to differing degrees of RFI.

Epoch	Sensitivity [μJy]	Beam size [mas]	Bandwidth [MHz]	Antennas involved
1	3	3.6×6.3	215	EfJbNtMcTrArWbOnGb
2	8	2.4×26.2	180	EfJbNtMcTrWbOnGb
3	3	3.6×10.0	200	EfJbMcTrArWbOnGb
4	7	2.2×26.6	200	EfJbMcTrWbOnGb

other two (Table 4.3).

4.2 Data reduction and calibration

As mentioned above, epoch 1 differs from all following ones in the respect, that it consists of only one big datafile. All later epochs are split into six different files corresponding to the six different correlation centers (Table 4.2). The data reduction and calibration process described below are essentially the same in all epochs (see Figure 4.2 for an overview). However, while in epoch 1 all calibration steps need to be performed on the entire dataset this is no longer necessary with the following epochs. As of epoch 2 it is sufficient to run all calibration steps only on the dataset correlated at the position of S1 (which is the in-beam calibrator) and to apply the derived solutions to the remaining five datasets later. This is possible because the pointing center and, thus, the atmosphere and the electronics the signal passed through are exactly the same in all six cases.

After correlation, all data is reduced, calibrated and imaged with using the NRAO Astronomical Image Processing System (AIPS[4]). The correlated data chunks of 1.9 GB size each are first loaded into AIPS using the task FITLD which combines them into one big set of visibilities. This task also sets up the initial calibration table (CL table) which we configured to have an entry every 15 seconds. The 'master file' contains data about all three sources – the target M15, the bandpass calibrator, and the phase reference source – that can be split out and worked on individually. The EVN pipeline[5] provides the first a priory calibration tables than can also be downloaded from the EVN archive. Of these tables, the flag table (FG table) containing information about band edges and off-source times, as well as the solution table (SN table) including system temperature and gain curve corrections are applied to the dataset as given yielding the first entries in the CL table. Parallactic angle corrections are applied with the task

4 http://www.aips.nrao.edu/
5 http://www.evlbi.org/pipeline/user_expts.html

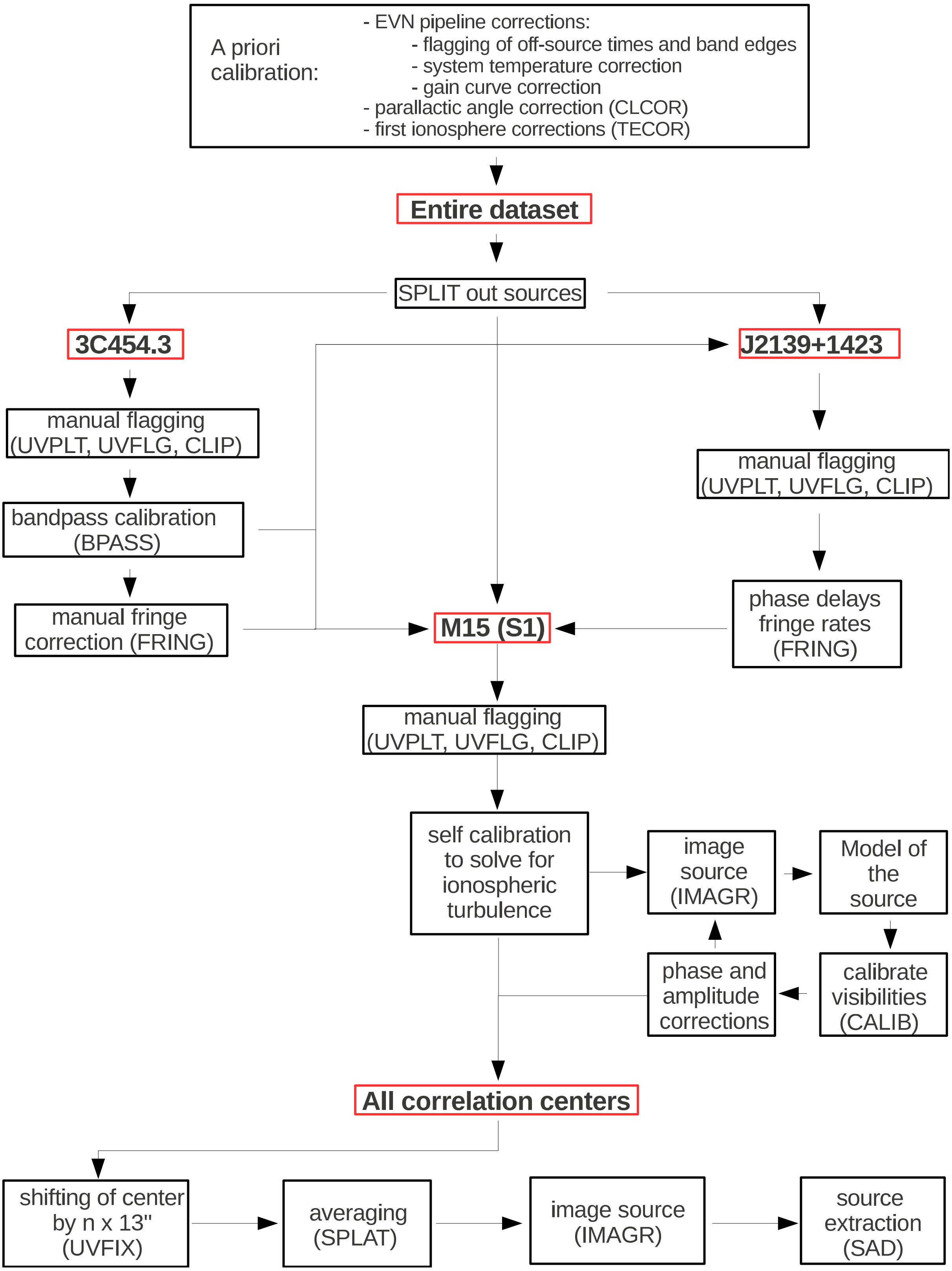

Figure 4.2: Schematic view of the calibration procedure. All calibration steps are performed on the S1-dataset (Table 4.2). The obtained solutions are combined into one calibration table that is copied and applied to all other correlation centers later (the entire dataset, epoch 1). See text for details.

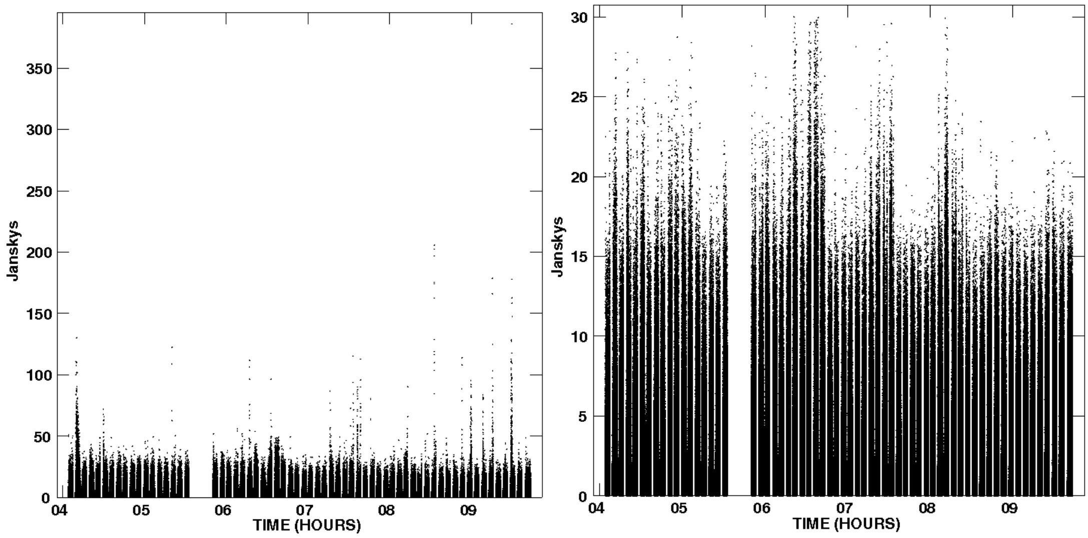

Figure 4.3: Visibility amplitudes of the target M15 as a function of scan time for all baselines and IFs. Left: Raw, uncalibrated data showing RFI. Right: After the removal of effected times and channels. Note the large difference in scale of the y-axes in both images.

CLCOR. Afterwards, we calculate first ionospheric corrections running TECOR with the Total Electron Content (TEC) maps published by the *Center for Orbit Determination in Europe*[6]. Even though these maps are quite crude in angular resolution (about 5°×2.5°) they have shown to be of use reducing the scatter in phase delay by a factor of 2-5 (Walker & Chatterjee 1999).

In a next step, major human interaction was required to identify and flag bad data and RFI for all antennas and subbands. The AIPS tasks employed in this step were UVPLT for identification and UVFLG and CLIP for flagging of bad visibilities. They key parameters used to tell 'bad' from 'good' visibilities were either far too high amplitudes (on the order of several hundred Jansky, Figure 4.3) or amplitudes systematically lower (very close or even equal to zero) than the average ones. To ensure optimal calibration the flagging was done on all three sources individually.

The bandpass calibration was done running BPASS on the data for 3C454.3 and yielded phase and amplitude gain factors for all 8×128 (512, epoch 1) channels for all antennas (saved in a BP table). After applying the BP table correcting for the frequency-dependent response of the bandpass (Figure 4.4b), we solve for the different phase delays between each of the eight subbands that is introduced by the different electronics the signals pass through. To this end, we perform a manual fringe correction running FRING on 3C454.3 on a sub-interval of about 30 seconds of observation. As in the entire calibration process, we chose the Effelsberg telescope as reference antenna because it is closest to being in the geographical 'middle' of the array. We

[6] downloaded from `ftp://ftp.unibe.ch/aiub/CODE/`

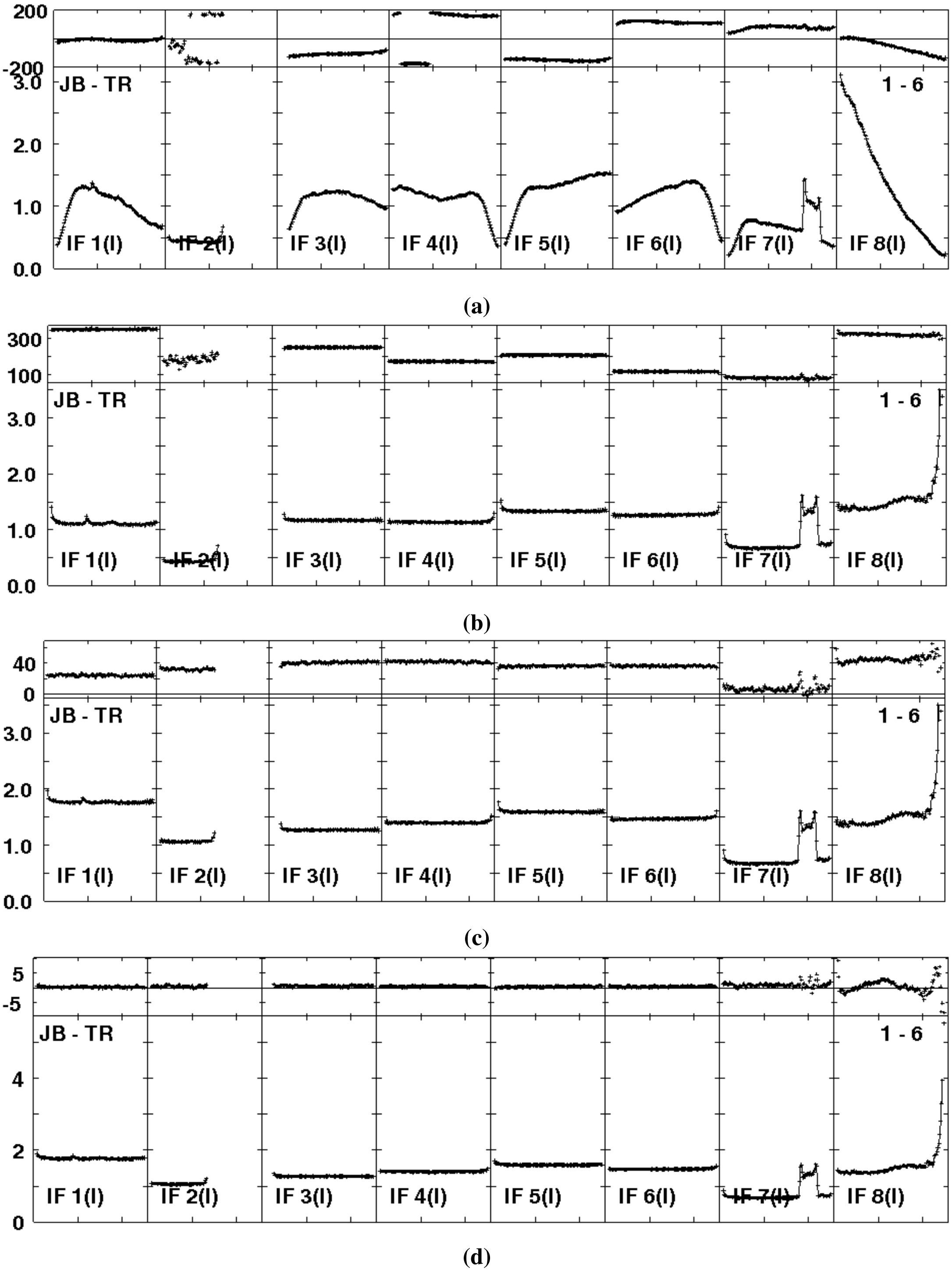

Figure 4.4: Outcome of the individual calibration steps performed on the phase calibrator for the Jb-Tr baseline in epoch 3. Plotted are the visibility phase in degrees (upper panel) and amplitude in Jansky as a function frequency. Each panel is divided into the individual eight IFs of 128 channels each. (a) A priori calibrated output from the correlator. The bandpass shape and phase jumps within and in between IFs are clearly visible. Slight slopes (fringe rates) are also obvious. (b) After application of the bandpass calibration that was performed on the bandpass calibrator 3C454.3. Amplitudes are flat and first phase slopes and phase jumps are removed. (c) After manual fringe fitting. Except for IF 7 phases are aligned across the band. (d) After fringe fitting the data. Phases now scatter around 0, all slopes and jumps are removed. IF 7 and 8 show RFI. The effected channels were flagged in all the data.

conduct the manual fringe correction twice because the Westerbork (Arecibo) telescope only takes part in the observation at the beginning (the end). In this step, we only solve for the phase delay but not for the phase rates. Thereby, we correct for constant phase offsets between the subbands and obtain continuous phase curves across the eight subbands of all antennas (Figure 4.4c).

At this point, we combine all SN tables obtained so far in one CL table and apply it to the data of the phase calibrator. We run FRING on this dataset including data over the entire time range. We solve for phase delays and phase rates simultaneously asking for solution intervals of about 1.5 minutes (which corresponds roughly to a typical scan length of the calibrator and is well within the coherence time at 1.6 GHz). After this, with all calibration tables applied, we check the outcome of the calibration process by inspecting the phase calibrator data with the help of the plotting task POSSM. We make sure that phases are continuous across all IFs and that they scatter closely around zero. If this is not the case or if amplitudes are non-flat but rise or fall off systematically (which is often the case towards the edges of sub-bands) the involved channels are flagged (Figure 4.4d).

The fringe solution tables are then combined with the latest CL table, the new flags are incorporated into the main FG table and both are then applied to the M15 data. In order to eliminate any residual phase delays and amplitude errors caused by the atmosphere we take advantage of the aforementioned strong source S1 and use it for in-beam calibration. In epoch 1 we had to first shift all (u,v,w)-coordinates to the position of S1 using the AIPS task UVFIX. In later epochs there was no need for this step. To speed up the self-calibration process we then average the visibilities both in the time- and frequency domain to 2 seconds integration time and 64 channels per IF, respectively. We obtained an initial model of the source through imaging with the task IMAGR that employs the Cotton-Schwab algorithm (Schwab 1984) which is a modified version of the original CLEAN algorithm (Högbom 1974). In the following, the first few strong CLEAN components are used in the task CALIB that calculates correction terms for all visibilities in order to meet the model. In this iterative process we solve for phases only first. The found solutions are applied in another IMAGR run producing a new model of the source with – in case of a successful CALIB run – an improved signal-to-noise-ratio (SNR). This new model is used in another CALIB run whose output SN table is then applied in the next IMAGR run. Once the SNR does not improve any further we use the latest (best) model and solve for phases and amplitudes simultaneously in a new CALIB run. In this fashion we were able to increase the SNR from the initial to the final model by a factor of up to 6 (Figure 4.5). The final CL table was obtained by merging the self-calibration SN table providing the best SNR with the CL table used prior to self-calibration. This master calibration table in conjunction with the

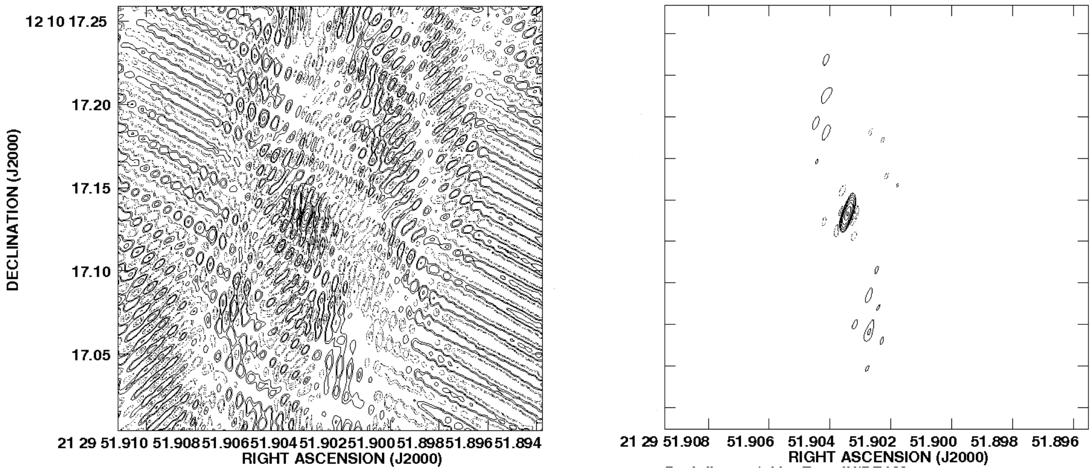

Figure 4.5: Contour plots of the strong in-beam source S1 before (left panel) and after (right panel) self-calibration in epoch 3. Contour levels are (-5, -3, 3, 5, 10, 20, 40, 80, 120) times the rms of the image after self-calibration. The SNR improved by a factor of 6.

bandpass and flag table were applied to all six datasets before final imaging.

4.3 Imaging and source extraction

It is impossible to construct an image of the entire FOV at our angular resolution of $\sim$ 3.5 mas. To properly sample the image plane with highest possible astrometric precision (assuming uniform weights) we need to have a pixel scale of about 0.8 mas/pixel. The largest possible size of an image supported by IMAGR, however, is 16384×16384 pixels resulting in an angular extent of the image of 13.1×13.1 arcseconds. Accounting for possible artefacts appearing at the edges of the images and in order to have a sufficient overlap between the individual images we decide to divide our FOV into tiles whose central coordinates are separated by multiples of 13 arcseconds in right ascension and declination. In total we thus need to shift the original (u,v,w)-coordinates 15×15 times to cover the entire FOV in epoch 1. As of epoch 2, each of the six correlation centers needs to be shifted 5×5 times. Therefore, before the actual imaging, we run UVFIX in a loop shifting the correlation center as described. However, we will investigate more optimal methods to maintain good astrometric precision (e.g. Morgan et al. 2011).

Since each shift of the dataset produces a new file of the same size as the original one ($\sim$11 GB) we need to reduce the amount of data. This is accomplished by averaging each shifted file as it was done during self-calibration. 2 seconds integration time and 64 channels per IF is also the maximal averaging we can afford not to loose astrometric precision and sensitivity towards the edges of each tile. Once the averaging is complete we delete the shifted file keeping the much smaller SPLAT file ($\sim$1 GB). After all shifts have been completed we image each file in another loop. Expecting the pulsar signals to be rather weak we perform the imaging by averaging over all subbands and channels and by applying natural weights to obtain optimal sensitivity. Since, in this weighting scheme, we do not achieve the highest angular resolution it is sufficient to have a pixel scale of 1 mas/pixel. In this way, we increase the overlap between individual tiles which later also helps to do cross referencing to eliminate false detections towards the outer edges of each image. We limit the number of CLEAN components (the parameter NITER) to a total of 1000 per image and set the flux limit (the FLUX parameter) to 10 (20) μJy corresponding to roughly 3σ in epochs 1 and 3 (2 and 4). In this way, the CLEAN algorithm either stops as soon as 1000 components have been found or if the maximal flux after subtraction of the CLEAN components is less than the set value.

Altogether, it took about 90 minutes for each tile to be shifted, averaged and imaged. Working on two tiles simultaneously the loop over all tiles still ran for about 1.5 weeks to complete the entire imaging. The bottleneck in this process is disk I/O speed – the more independent disks are involved the faster the run. In general one can say that per CPU-core available for computation one independent hard drive is needed.

Considering the size and the amount of images produced, manual inspection for source extraction is unfeasible. Hence, we employ the AIPS task SAD in another loop over all images to extract possible sources. In SAD one can chose to search for objects with certain flux densities or, alternatively, one can set a SNR-level down to which the images are scanned. Because of different noise and slightly different absolute flux levels in the different epochs we chose the latter option for better comparability. For SAD to run in this mode it needs both a noise map of the image and the image itself. Therefore, before running SAD, we produce a noise map of each tile with the task RMSD. Expecting a rather homogeneous noise background throughout the images we produce low-resolution rms-maps such that the image is sampled at steps of 256 pixels in X- and Y-direction. Allowing for smooth transitions and sufficient overlap between the steps the rms-value is calculated in boxes of 1024×1024 pixels. We set the SAD-parameters such that each image is scanned multiple times to look for sources having SNRs of 20, 10, 7, 5, and 3. The outcome of this search is a table with roughly 38000 entries per tile. On average, 15 of these entries have SNR$\geq$ 5, 2000 have SNR$\geq$ 4, and the remaining entries are pixels with SNR$\geq$ 3. Obviously, it is absolutely improbable to have such a vast amount of detections per 16×16 arcseconds and, hence, most of the entries can be attributed to Poisson noise. Nevertheless, there is a chance that some of the entries are real.

With four observational epochs at hand it is easy to cross-check positions of sources detected using SAD. The direct output of SAD, however, is unpractical for this task because source positions are given as distances (in right ascension and declination) from the tile center of the tile the sources where detected in. Therefore, we wrote a code that converts the distances to the individual tile centers to distances from the assumed cluster center (the pointing center) and then cross-correlate all entries in all four epochs. In between subsequent epochs we allow for a positional inaccuracy (or positional change due to proper motion and/ or parallax) of 15 mas corresponding to roughly four times the beam width in right ascension.

5 Results

The results presented here are preliminary since not all of the six planned observations had been conducted at the time of writing. Nevertheless, even though only four data sets were available for the analysis, the aims of this project could already be addressed. In fact, we were able to detect two of the eight known MSPs and the LMXB AC211 in M15 at a high signal-to-noise ratio throughout the epochs.[1] Therefore, we could trace their motion across the sky and determine first proper motion results. Furthermore, we present follow-up observations of the unclassified source S1 that was previously detected by Machin et al. 1990, Johnston et al. 1991, and Knapp et al. 1996. We also provide first new data on an object we dubbed T169 that only Knapp et al. 1996 report to have detected previously. Finally, we can put an upper limit on the flux density of the assumed central IMBH-candidate in M15 at 1.6 GHz.

5.1 Proper motion results

5.1.1 15A, 15C, AC211

After successful calibration and shifting of the data we first searched for the already known sources in M15. To that end, we imaged the appropriate tiles at the positions of the eight known MSPs and the LMXB as they are published on the website of the *SIMBAD Astronomical Database*[2]. We imaged the UV-data in IMAGR in interactive mode applying boxes to the strongest peak close to the expected positions. In this way we eliminated side-lobes and recovered most of the targets' fluxes. Unfortunately, we did not detect all of the known MSPs but only two of the strongest ones which are PSR J2129+1210A and PSR J2129+1210C (hereafter referred to as 15A and 15C, respectively). Additionally, we also observe the LMXB AC211 at high SNR. Two of these three objects (15A and AC211) are very close (within 4.5 arcsec corresponding to ~ 0.25 pc, Figure 5.1) to the assumed core of M15 and, thus, are potential candidates to detect high peculiar velocties within the cluster's gravitational potential. Our observations of 15C provide the first VLBI-detection of the double neutron star system 15C.

Figure 5.2 depicts the measured integrated flux densities (results of a Gaussian fit to a point

[1] The MSP J2129+1210C became fainter in between epochs until it disappeared entirely as of epoch 4.
[2] `http://simbad.u-strasbg.fr/simbad/`

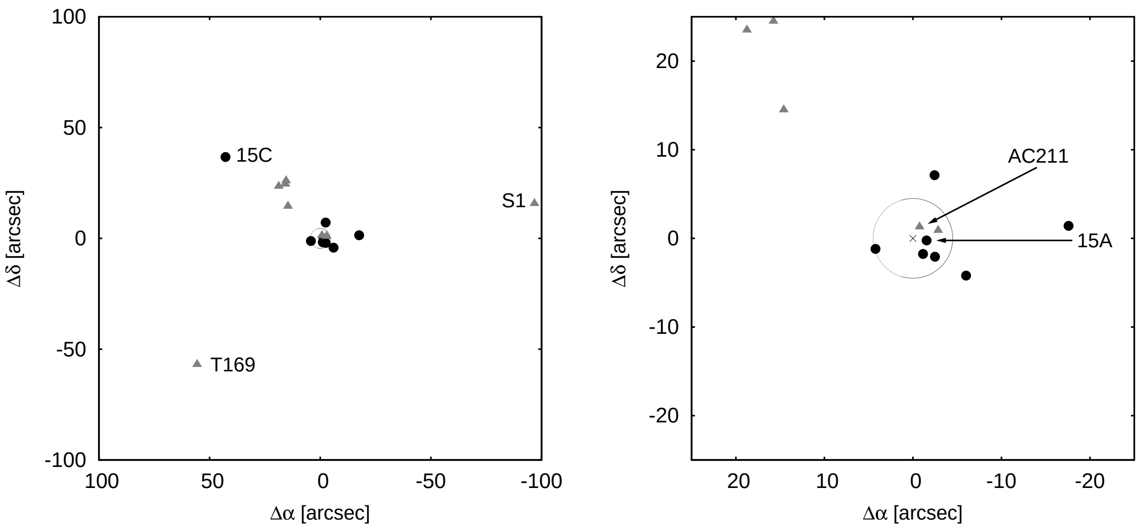

Figure 5.1: Positions of known radio sources relative to the pointing center (indicated by the cross). Left: Approximate field of view of the array. Right: Zoom in on the central 50×50 arcsec. In both figures we highlight the sources that we detected. Dots represent the known Pulsars while triangles are other objects like planetary nebulae, unclassified sources and X-ray binaries. The circle has a radius of 4.5 arcsec.

source at the positions of each source with the AIPS task IMFIT; exact numbers and the corresponding SNR based on the local rms are listed in Table 5.1, errors listed are those from the fit). Note that epochs 2 and 4 lacked the Arecibo telescope and, hence, the noise background is higher by about a factor of 2 (Table 4.3). The measured flux density of 15A varies considerably in between epochs and is still under investigation. In the case of 15C the measured flux densities and SNRs go down steadily until 15C was no longer detectable in epoch 4.[3] AC211 appears to become brighter between epochs which seems to correlate with the X-ray activity of M15 as a whole (Figure 6.2). Furthermore, in the data of AC211 we observe two components in epoch 3 (discussed below, Figure 5.3c). In Table 5.1 we only list the flux density and SNR of the southern component (comp 1) since both components are very similar in strength.

Tables 5.2 and 5.3 list the measured positions (as determined with the Gaussian fit mentioned above) of 15A, 15C and of AC211, respectively. For AC211 the positions of both components in epoch 3 are listed. We used these coordinates to determine relative changes in the positions of each source in between epochs. Figure 5.3 depicts the outcome of this analysis where all changes are plotted relative to the position as it was measured in epoch 1 which is defined to be at the origin of the coordinate system. For 15A and 15C (Figures 5.3a and 5.3b, respectively) we

[3] In long-term observation with the Arecibo telescope 15C becomes undetectable at about the same time as in our observations (P. Freire, private communication). See Section 6.1 for a discussion.

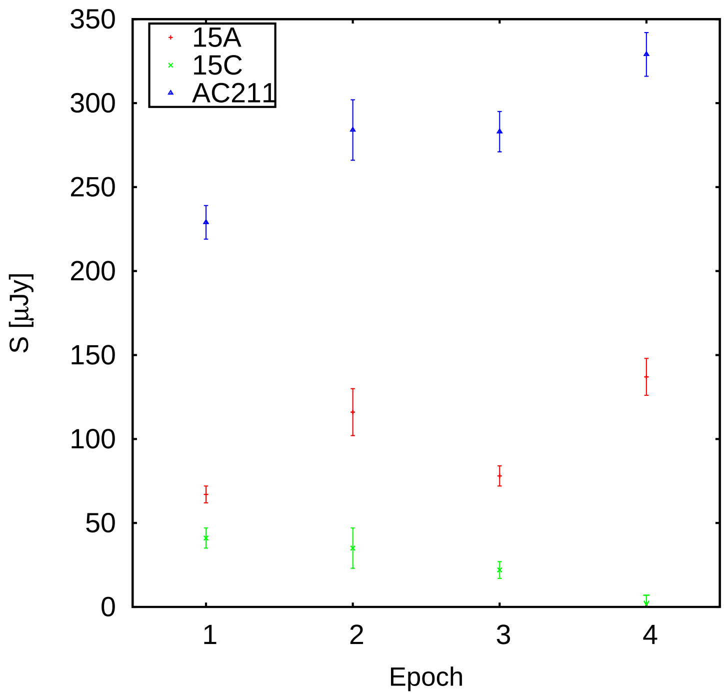

Figure 5.2: Measured flux densities of 15A (red), 15C (green), and AC211 (blue) in all epochs. Note the steady decreas in flux density for 15C. In epoch 4 only an upper limit for the flux density of 15C can be given.

also plot their positions extrapolated by the proper motion results as determined through pulsar timing by Jacoby et al. 2006 (Table 6.2). Our measured positions of 15A and 15C lie within the extrapolated 1σ-errors of Jacoby et al. 2006. However, for 15C we detect an improbable shift in position from epoch 1 to 2 not following the global motion of M15 at all. The same phenomenon is observable for S1 (Figure 5.5a) in between epochs 1 and 2. We believe that these shifts are a result of the different observing and correlation strategy in epoch 1 (chapter 4.1). The MSP 15C and the source S1 are located at rather large distances (55.6″and 94.6″, respectively, Figure 5.1) from the phase tracking center (which coincides with the assumed cluster center) and, therefore, prior to imaging we needed to shift the (u,v,w)-coordinates by large amounts in epoch 1. According to Morgan et al. 2011 the task UVFIX introduces image registration errors on the order of ~ 1 pixel per 10^4 shifted pixels. For 15C (S1) this corresponds to astrometric errors on the order of $\pm 4.1(\pm 9.4)$ mas in right ascension and $\pm 3.6(\pm 1.5)$ mas in declination. Due to these inaccuracies the data from epoch 1 in the proper motion analysis of 15C and S1 has very little weight. However, the astrometric accuracy of 15A and AC211 is not influenced by this effect because both sources are within 4.5 arcsec of the pointing center. In order to improve the astrometry of 15C and S1 in epoch 1 we will reanalyse the data after impementation of a more accurate shifting algorithm (e.g. the one proposed by Morgan et al.

2011). For now, however, we cannot put very tight constraints on the proper motion of 15C

Table 5.1: Signal-to-noise ratios and integrated flux densities, S, of the detected classified sources at the individual epochs.

	15A		15C		AC211	
Epoch	S [μJy]	SNR	S [μJy]	SNR	S [μJy]	SNR
1	67(5)	22.4	41(6)	11.1	229(10)	30.9
2	116(14)	14.9	35(12)	4.8	284(18)	25.6
3	78(6)	22.7	22(5)	7.5	283(12)	35.7
4	137(11)	20.3	≤ 7		329(13)	42.2

Table 5.2: Positions of the detected known pulsars in M15. Values in brackets are 1σ-errors in the last digit.

	15A		15C	
Epoch	Ra	Dec	Ra	Dec
1	$21^{h}29^{m}58\overset{s}{.}246557(5)$	$12°10'01\overset{''}{.}2337(1)$	$21^{h}30^{m}01\overset{s}{.}2038(3)$	$12°10'38\overset{''}{.}163(4)$
2	.24649(1)	.2333(8)	.20349(3)	.165(3)
3	.24644(1)	.2325(2)	.20344(2)	.1591(5)
4	.24597(1)	.228(1)		

Table 5.3: Positions of the LMXB during the epochs. Values in brackets are 1σ-errors in the last digit. For epoch 3 coordinates for both component 1 and component 2 as seen in Figure 5.3c are given.

	AC211	
Epoch	Ra	Dec
1	$21^{h}29^{m}58\overset{s}{.}312540(4)$	$12°10'02\overset{''}{.}6818(2)$
2	.312458(6)	.6832(4)
3	.312491(4)	.6733(1)
	.312390(4)	.6870(2)
4	.312371(4)	.6783(3)

because epoch 1 is systematically effect by the UVFIX-algorithm, epoch 2 suffers from a lack of the longest baselines to Arecibo and from RFI, and we have no data for epoch 4.

For the low mass X-ray binary AC211 we observe an unexpected positional shift in epoch 3. Figure 6.1 shows a contour plot of this target where a very clear bipolar structure in the North-South direction becomes obvious. Epoch 3 is one of the epochs with a higher noise level and it could easily be that this bimodal structure is merely a result of a noise peak at the exact position

Table 5.4: Proper motion results for the classified sources as determined from the linear fits in Figure 5.4.

	μ_α [mas/yr]	μ_δ [mas/yr]
15A	-2.5(1)	-2.9(7)
15C	-2.9(13)	-12.5(87)
AC211	-2.1(2)	-3.6(12)

of AC211 smearing out its flux over two side-lobes. A second possibility, namely that systematic effects resulting from false calibration cause this structure can be excluded because 15A is detected as a point source even though it is only ~ 1.7 arcsec to the South-West of the LMXB. However, at this stage it cannot be ruled out that this bipolar structure is real and results from a short-term outburst of the source. This explanation will be discussed further in chapter 6.4. In the proper motion analysis of AC211 we do not exclude the data from epoch 3. Instead, we calculate the weighted mean position of both components and add their error estimates in quadrature (the position is indicated by the black diamond in Figures 5.3c and 5.4). In the proper motion fit for this source we use this estimated central position and ignore the positions of the individual components.

In Figure 5.4 we plot for each of the targets the relative positional offsets in right ascension and in declination separately as a function of time. Similar to Figure 5.3 we define the origin of the coordinate systems to coincide with the data from epoch 1. At the distance of M15 ($\sim 10.3 \pm 0.4$ kpc) we are insensitive to the influence of its parallax $\pi \sim 0.1$ mas on the measured position. Therefore, to extract the objects' proper motion across the sky we apply a simple weighted linear least squares fit of the form

$$f(t) = a * t + b \tag{5.1}$$

separately to both right ascension and declination. In the fit each data point is assigned a weight $w = 1/z^2$ according to its error z at observation time t. The parameter a obtained in this scheme corresponds to the proper motion in mas/yr and the parameter b is of no further interest. It is close to zero through the choice of the coordinate system. The error z of each data point was taken to be equal to the positional error as listed in Tables 5.2 and 5.3. These errors are based on the beam size (BS) and the signal-to-noise ratio in each epoch and were estimated according to $z \approx SNR/(2 * BS)$. In epoch 1 the astrometric inaccuracies introduced in UVFIX for 15C are included as discussed above. Table 5.4 summarizes the results of these fits for the proper motion in right ascension, μ_α, and in declination, μ_δ. The errors stated are taken as determined from the weighted least squares fit.

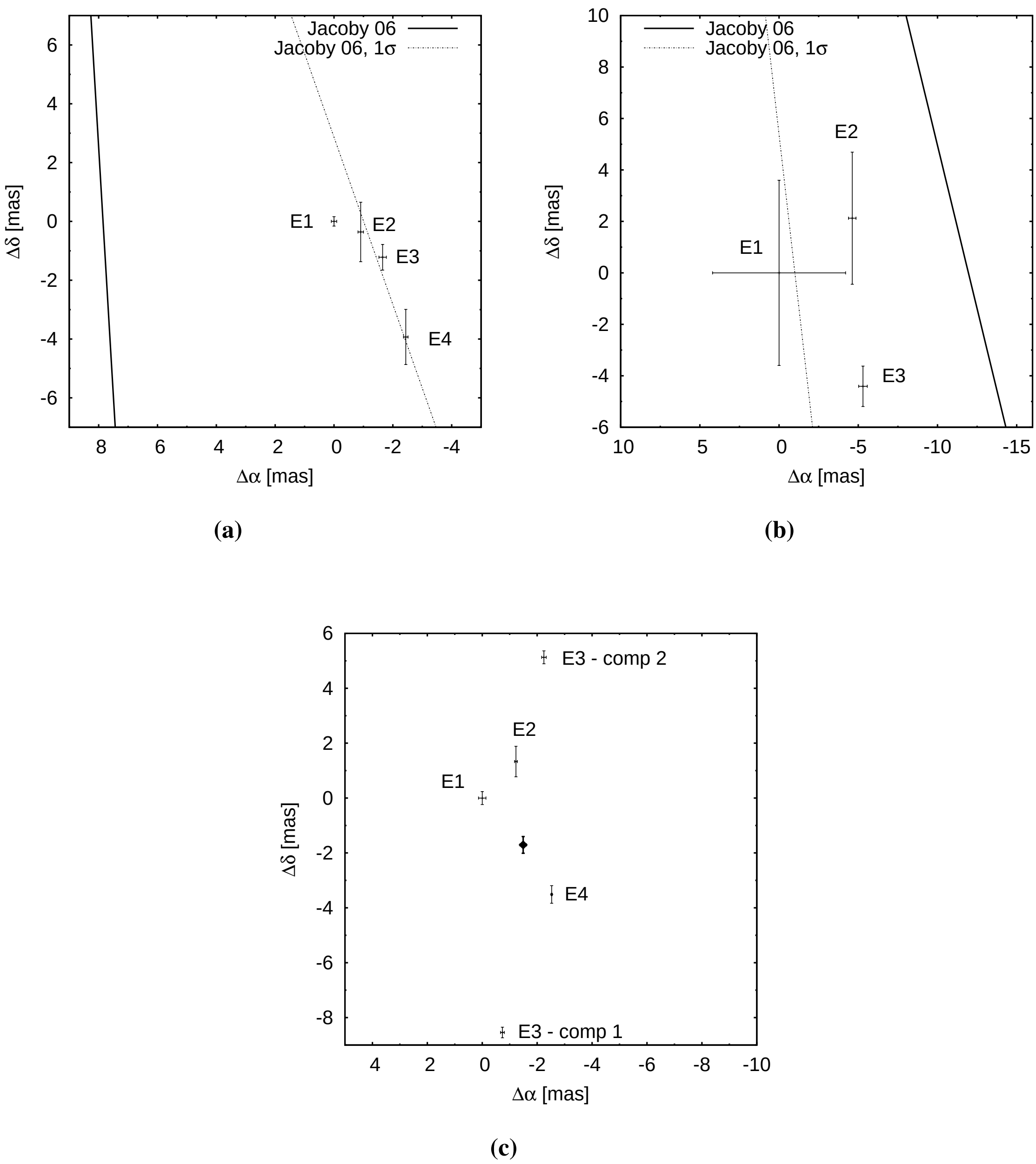

Figure 5.3: Apparent change in position in between epochs for (a) 15A, (b) 15C, (c) AC211. The measured positions in epoch 1 are defined to be the origin of each coordinate system. In (a) and (b) we also plot the positions extrapolated by the proper motion results as found through pulsar timing by Jacoby et al. 2006. The large jumps between epochs 1 and 2 in (b) are most likely systematic effects introduces by shifting the (u, v, w)-coordinates in UVFIX in epoch 1. The diamond in (c) indicates the middle between components 1 and 2 in epoch 3. See text for further details.

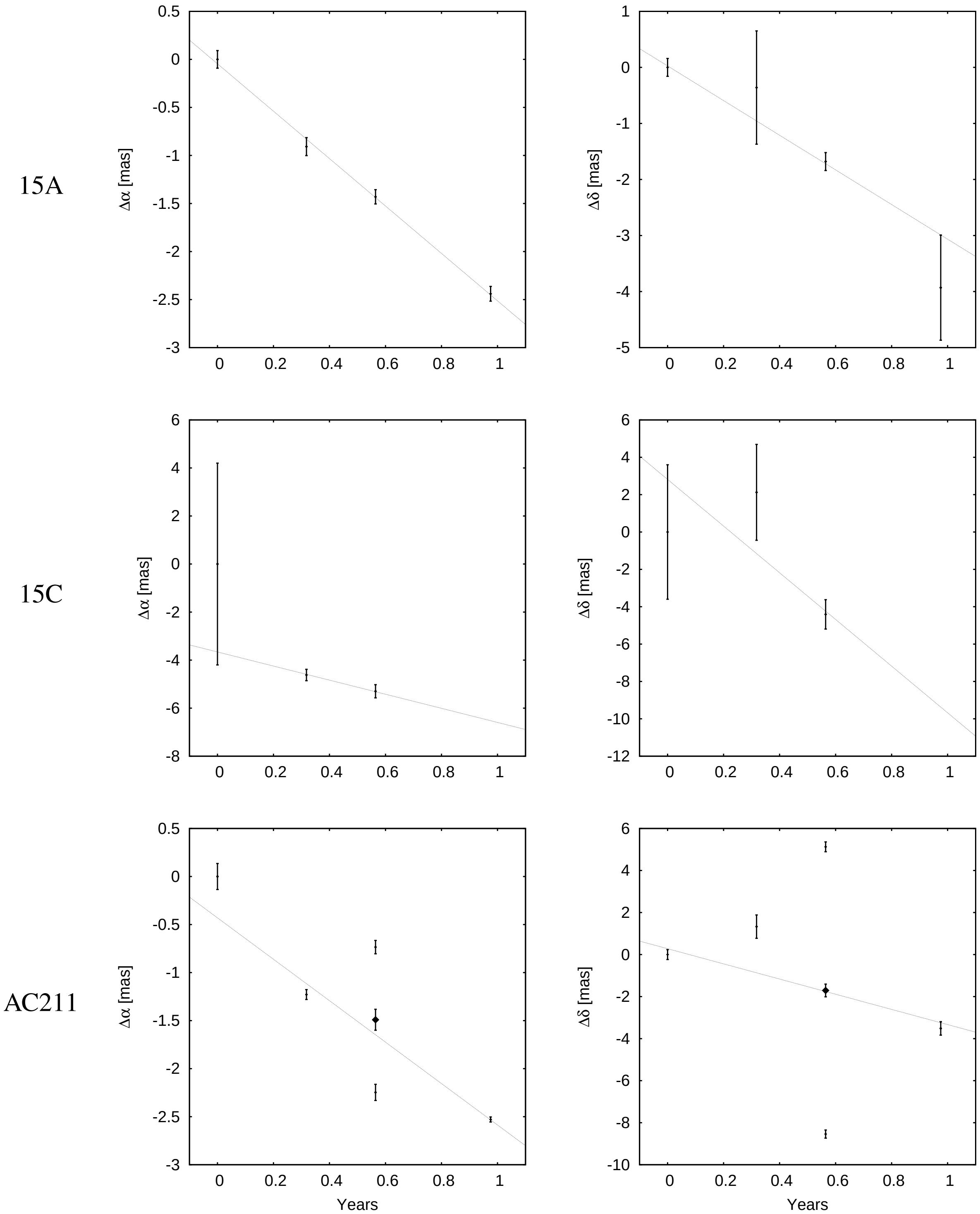

Figure 5.4: Apparent positional change in right ascension (left column) and in declination (right column) as a function of time. The data points were fitted with a weighted linear fit to determine the proper motion. The diamond in the plots for AC211 indicates the middle between components 1 and 2 in epoch 3 and was used as a data point in the fit (the individual components were ignored). Results are summarized in Table 5.4.

Table 5.5: Signal-to-noise ratios and integrated flux densities of S1 and T169 at the individual epochs.

	S1		T169	
Epoch	S [mJy]	SNR	S [mJy]	SNR
1	2.42(6)	84.8	0.17(3)	9.8
2	3.37(6)	88.3	0.3(1)	4.6
3	2.80(5)	118.3	0.11(1)	16.1
4	2.75(6)	78.0	0.28(2)	24.8

5.1.2 S1 and T169

Apart from the three classified sources discussed above, we also detect the unclassified sources S1 and T169 at high SNR. We perform an analysis similar to the one described above also for these two objects. Both sources have been detected before,[4] but none of these authors was able to tell whether or not S1 and T169 are part of M15.

In Table 5.5 we list again integrated flux densities and corresponding SNRs of both objects. Except for epoch 2 S1 has a consistent flux density in between epochs while the flux density of T169 varies by a factor of up to 3. The reason for this is still unclear and the apparent variability needs to be confirmed in later epochs. We also list the measured positions of both targets in Table 5.6. As discussed above, in epoch 1 the position of S1 carries rather large uncertainties introduced through the task UVFIX. The same holds true for T169 since it is located at an angular distance of ~ 79 mas towards the southeast of the cluster core. As a result, systematic astrometric errors of $\sim \pm 5.4$ (± 5.7) mas in right ascension (declination) were carried along in epoch 1. In all following epochs this effect can be neglected because the correlation centers S1 and VRTX3 (Table 4.2) almost coincide with the coordinates of S1 and T169, respectively.

Figure 5.5 depicts the apparent relative change of coordinates of both targets during the epochs. For S1 (Figure 5.5a) two things become obvious: First of all we observe a large jump in position between epoch 1 and 2 that is inconsistent with the apparent motion in later epochs. It is, however, consistent with the observed jumps for 15C and also for T169 which supports the notion that this a systematic effect as discussed above. Secondly, as of epoch 2 S1 follows what seems to be a straight line. Decomposing the positional change in right ascension and declination and plotting both as a function of time (Figure 5.6 top panels) reveals that S1 follows a similar trajectory as the three known sources discussed above (Figure 5.4). Applying a similar weighted linear fit as before (Equation (5.1)) yields a proper motion (Table 5.7) comparable to

[4] In fact, S1 has been observed at 1.4, 4.9, and 8.4 GHz by Machin et al. 1990, Johnston et al. 1991, and Knapp et al. 1996, respectively. The latter also observed T169: It is their source number 3 in NGC 7078.

Table 5.6: Positions of the unclassified sources S1 and 169 in epochs 1 to 4. Values in brackets are 1σ-errors in the last digit. The large errors in epoch 1 result from large shifts as discussed in Section 5.1.

	S1		169	
Ep	Ra	Dec	Ra	Dec
1	$21^h29^m51\overset{s}{.}9029(1)$	$12°10'17\overset{''}{.}133(9)$	$21^h30^m02\overset{s}{.}0859(4)$	$12°09'04\overset{''}{.}197(6)$
2	.903443(2)	.1344(1)	.08608(4)	.230(3)
3	.9034263(5)	.13328(2)	.085693(8)	.2240(3)
4	.9033851(8)	.13234(5)	.085692(4)	.2185(3)

the ones of 15A, 15C, and AC211 (Table 5.4).

The case of T169, however, is not as conclusive (Figures 5.5b and 5.6 lower panels). In right ascension we observe large jumps from epoch 1 to 2 and from epoch 2 to 3 but hardly any change in right ascension from epoch 3 to 4. In Declination, on the other hand, the inconsistent movement from epoch 1 to 2 is observable as expected and the source seems to follow a rather straight trajectory as of epoch 2. Therefore, we only fit the declination excluding the data from epoch 1 to obtain a proper motion result and leave the right ascension for reconfirmation in later epochs. The results are summarized in Table 5.7.

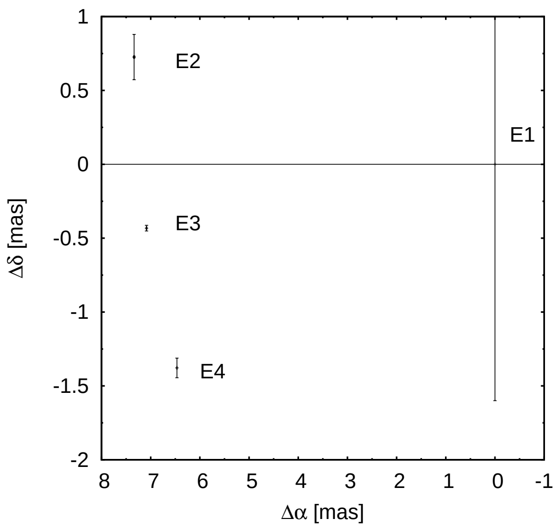

(a)

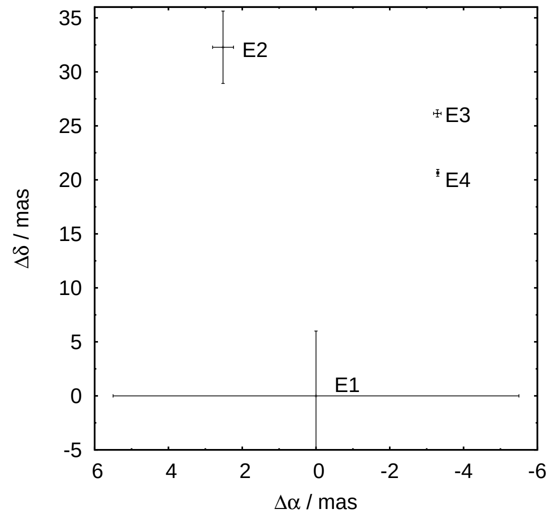

(b)

Figure 5.5: Apparent change in position in between epochs for (a) S1, and (b) T169. The measured positions in epoch 1 are defined to be the origin of each coordinate system. The large jumps between epochs 1 and 2 are most likely systematic effects introduces by shifting the (u, v, w)-coordinates in UVFIX in epoch 1.

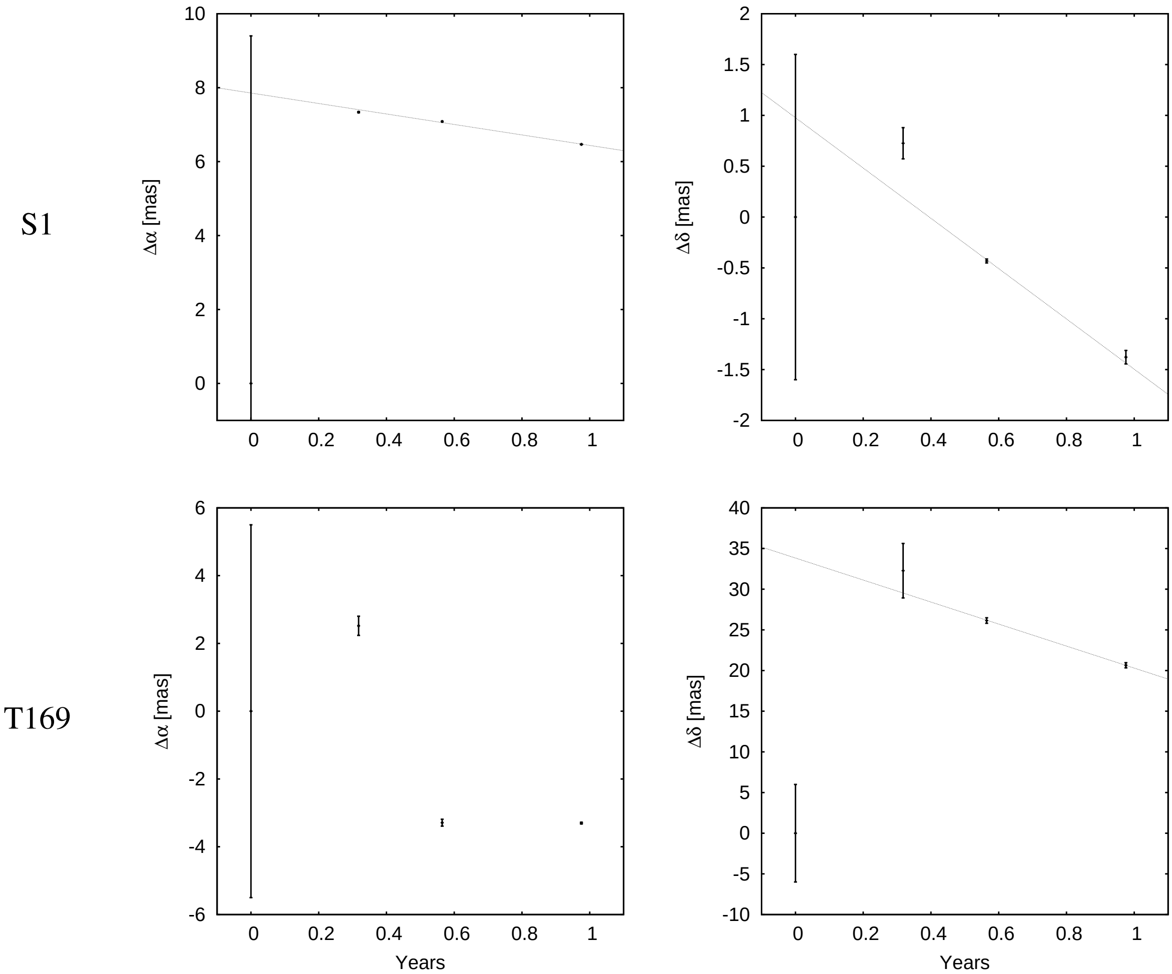

Figure 5.6: Apparent positional change in right ascension (left column) and in declination (right column) of S1 (upper panels) and T169 (lower panels) as a function of time. The data points were fitted with a weighted linear fit to determine the proper motion.

Table 5.7: Proper motion result for S1 and T169 as determined from the linear fit in Figure 5.6. In the fit for T169 we excluded the data from epoch 1.

	μ_α [mas/yr]	μ_δ [mas/yr]
S1	-1.4(1)	-2.5(4)
T169	–	-13.5(9)

5.2 On the central IMBH - candidate of M15

Figure 5.7 displays contour plots of the central region of M15 for all four epochs. All tiles are centered on the pointing center at coordinates RA = $21^{\mathrm{h}}29^{\mathrm{s}}58\overset{\mathrm{s}}{.}3500$, DEC = $12^\circ10'01\overset{''}{.}500$ and have dimensions of 0.5×0.5 arcsec. It is obvious that we do not detect a significant signal at 1.6 GHz down to our sensitivity limit of ~ 3 (7) μJy in epochs 1 and 3 (2 and 4). Therefore, we can put an upper 3σ limit of 10 μJy on the radio flux density at 1.6 GHz of a possible central source.

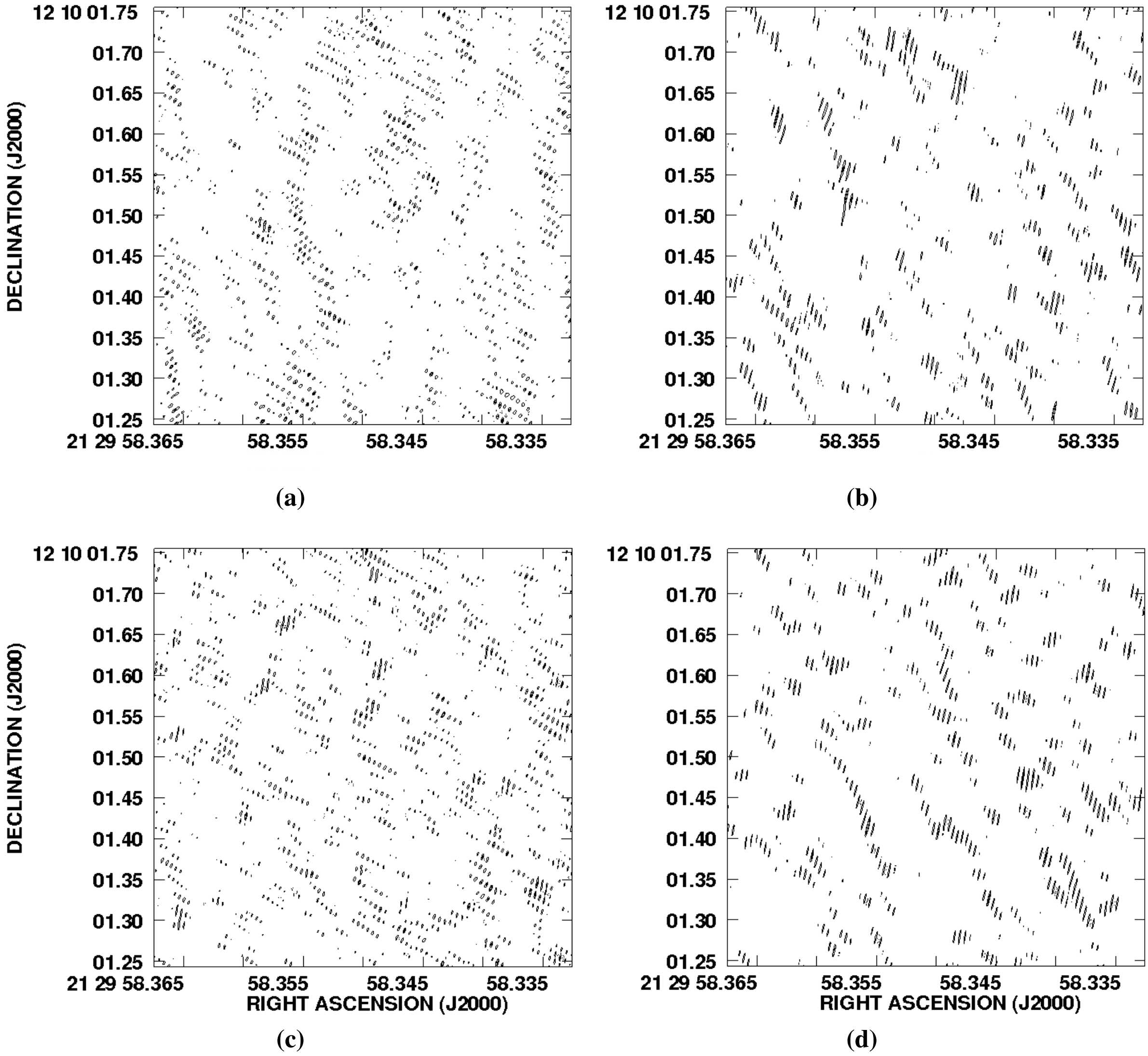

Figure 5.7: Contour plots centered on the assumed core of M15 (coincides with the pointing center) for epochs 1 to 4 (a to b). Each tile has a dimension of 0.5×0.5 arcsec. Contours are $(-5, -3, 2, 3, 5)$ times the rms in each individual epoch (Table 4.3).

6 Discussion

6.1 Fading away of 15C

Within the course of one year the double neutron star system (DNS) 15C slowly faded away to become undetectable for our array in November 2010. As mentioned above, single dish observations with the Arecibo telescope confirm the disappearance of 15C (P. Freire, private communication) and, thus, we are certain that this is not an effect due to faulty calibration.

The most likely explanation for the observed behaviour is geodetic precession caused by the misalignment of the orbital angular momentum vector of the binary system and the spin angular momentum vector of the MSP itself. This effect, predicted by General Relativity, arises because space-time is curved by the companion's gravitational field. As a results, the rotational axis of the NS precesses during its orbit about the companion star. Experimental evidence for this scenario is given, e.g., by observations of the DNS PSR B1913+16 (Weisberg et al. 1989, Kramer 1998) and the binary system PSR J1141-6545 (Hotan et al. 2005, Manchester et al. 2010). Since 15C is in a binary orbit with another NS the same phenomenon could also be at work in this case.

Assuming GR is the correct description of gravity, Barker & O'Connell (1975) presented a time averaged expression for the spin precession rate Ω_p of a pulsar with mass m_p in a binary orbit with a companion of mass m_c

$$\Omega_p = \frac{1}{2}\left(\frac{G}{c^3}\right)^{2/3}\left(\frac{P_b}{2\pi}\right)^{-5/3}\frac{m_c(4m_p+3m_c)}{(1-e^2)(m_p+m_c)^{4/3}}\,. \tag{6.1}$$

Here, G, c, P_b, and e are Newton's gravitational constant, the speed of light, the binary period of the system, and the orbit's eccentricity, respectively. Using the values for 15C as they are listed in Jacoby et al. 2006 (Table 6.1) we compute a value of $\Omega_p \approx 1.30°\mathrm{yr}^{-1}$. This result is too small for an entire beam to move out of our line of sight within one year. Nevertheless, given the very sharp pulse profile of 15C and its relatively low flux density (Anderson et al. 1990, Table 5.1) it is quite likely that, until now, we have been struck by the outer edge of the beam only. Thus, during our observations the rotational axis of the MSP might have precessed far enough such

Table 6.1: Parameters of the DNS 15C used in Equation (6.1). All values were adopted from Jacoby et al. 2006.

Pulsar mass, m_p [$M_\odot$]	1.358(10)
Companion mass, m_c [$M_\odot$]	1.354(10)
Orbital period, P_b [days]	0.33528204828(5)
Orbit eccentricity, e	0.681395(2)

that the beam of emission moved out of our line of sight.

6.2 Implications of proper motion results

Table 6.2 summarizes the proper motion results of all detected sources. For comparison we also list the proper motion results based on pulsar timing as they were published by Jacoby et al. 2006 (in the following referred to as J+06). Our results agree with the published ones within the error bars. However, we note that our values for μ_α are systematically higher than those of J+06. Since our values for all detected cluster members are consistent with one-another we are confident that they are robust. The data of J+06 is based on pulsar timing and, hence, the discrepancy between ours and their results could be caused by the timing model they apply.

When comparing the proper motion results of S1 with those of the other sources it becomes quite obvious that S1 must be part of the globular cluster. Furthermore, its proper motion results are slightly lower than those of 15A and AC211. These results for S1 are, however, largely consistent with those of 15C published by J+06 (and also with ours considering the large uncertainties in the results for 15C). Keeping in mind that, compared to the other targets, 15C and S1 are far away from the assumed cluster center (Figure 5.1) it is fair to argue that those two sources are the best indicators for the global motion of M15. 15A and AC211, on the other hand, might exhibit peculiar motion within the cluster potential. As a toy model, we assume μ_α and μ_δ of 15C and S1 to represent the global motion of M15 and take the weighted mean of both values (for 15C we adopt the results of J+06 since ours carry too large an error). With this simple approach we obtain $\mu_\alpha^g = -1.4(1)$ mas/yr and $\mu_\delta^g = -2.5(4)$ mas/yr for the global proper motion in right ascension and declination. Subtracting these values from the proper motion of 15A and AC211 yields transverse peculiar velocities of 59(17) and 61(20) km/s, respectively. Both values are above the cluster escape velocity $v_{esc} = 40.9$ km/s (Evans et al. 2003).

The nature of T169 is still inconclusive because it could be both a foreground source and a member of M15. The apparent motion of T169 in declination suggest that is moves along an apparent straight trajectory (Figure 5.6). Its motion along right ascension, on the other hand, is

Table 6.2: Summary of the proper motion results of all sources. For comparison the pulsar timing results from Jacoby et al. 2006 are also given.

	This Work		Jacoby et al. 2006	
	μ_α [mas/yr]	μ_δ [mas/yr]	μ_α [mas/yr]	μ_δ [mas/yr]
15A	-2.5(1)	-2.9(7)	-0.26(76)	-4.4(15)
15B	–	–	1.7(33)	-1.9(59)
15C	-2.9(13)	-12.5(87)	-1.3(5)	-3.3(10)
AC211	-2.1(2)	-3.6(12)	–	–
S1	-1.4(1)	-2.5(4)	–	–
T169	–	-13.5(9)	–	–

irradic and needs to be constrained further in later epochs. At the distance of M15, however, T169's proper motion in declination would translate to a transverse velocity of 657(44) km/s. Assuming T169 to be a member of M15 we can subtract its global proper motion. Nevertheless we still obtain a rather large value of 536(44) km/s. Considering the large distance of T169 from the cluster center it is very improbable that the object has such a large peculiar velocity. Therefore, we conclude that T169 is most likely not a member of the globular cluster. Note, however, that this conclusion is only preliminary and needs to be confirmed or rejected with the data from later epochs.

6.3 The nature of S1 and T169

The source S1 has been detected at various radio frequencies but the measured flux densities have not allowed for a conclusive characterization of the object. Table 6.3 lists literature values for the source's flux density which reveal that the object seems to be variable. Our results support this notion because we observe varying flux densities between epochs 1, 2, and 3. J+06 deduced a positiv spectral index $\alpha = +0.4$ from measured flux densities at 1.4 and 4.9 GHz. They noted, however, that such a spectral index is rather unusual for an extragalactic source. With the data at hand we know that S1 is not an extragalactic source and that it is variable on time scales of a few months. Assuming that the data at 4.9 GHz was taken at a time when the source was in a more active state we ignore it for the time being and compute $\alpha \approx +0.2$ under the assumption that the data at 1.4 / 1.6 GHz and at 8.4 GHz were taken at a similarly active state. Such an almost flat spectrum indicates optically thick synchrotron emsission (e.g. Migliari et al. 2010) which, in turn, implies that the source of emission could be an X-ray binary. However, in order to confirm this interpretation X-ray observations are needed.

For T169 there is not as much spectral information available as for S1. Nevertheless, our measurment at 1.6 GHz in conjunction with data from Knapp et al. 1996 also imply a rather flat

Table 6.3: Flux densities of S1 and T169 at different frequencies.

ν [GHz]	S [mJy] S1	S [mJy] T169
1.4 [a]	3.28	–
1.6 [b]	2.42-3.37	0.11-0.30
4.9 [a / c]	5.65 / 7.0	–
8.4 [d]	4.69	0.23

[a] Johnston et al. 1991, [b] this work
[c] Machin et al. 1990, [d] Knapp et al. 1996

spectrum in the radio regime. However, as shown in our data T169 seems to be variable on time scales of a few months and the flux densities measured at different epochs might not be comparable. Given its Galactic origin, however, T169 could also be an X-ray binary.

6.4 The bipolar structure of AC211 in epoch 3

Figure 6.1 left shows a contour plot of AC211 in epoch 3. The structure is elongated in North-South direction with a slight offset also in right ascension. In total, the two peaks are separated by roughly 13.7 mas which is slightly larger than the beam size of 10 mas in declination. The direction of the elongation is almost in direction of the beam but not entirely. For comparison we also give a contour plot of 15A in epoch 3 in the right panel of Figure 6.1. 15A is located at 1.7 arcsec to the South-West of AC211 and should – in case of systematic errors in the calibration – exhibit the same structure. Since this is not the case we can exclude systematic effects causing the morphology.
Furthermore, given the dimension and high resolution of the FOV, the chance of a noise peak to contaminate the image at the exact position of AC211 can be considered to be quite low.

Therefore, we conclude that the observed bipolar structure could be real and might be caused by an outburst that occurred at some time between epochs 2 and 3. As a matter of fact, Charles et al. 2002 report to observe variability of the source in X-ray data spanning 5 years. Furthermore, the X-ray data published by the *MAXI* mission[1] (Matsuoka et al. 2009) reveals X-ray variability of M15 during our observations that could be caused by the activity of AC211 (Figure 6.2).
At the distance of M15 the angular separation between the components corresponds to about 137 AU. The time span from epoch 2 to 3 is 110 days, the one from epoch 3 to 4 is 150 days. Assuming that the outburst occurred shortly after epoch 2 the transverse velocity v of the ejected material (ejected from an object in the middle of both components) would be roughly 0.6 AU

[1] `http://maxi.riken.jp`

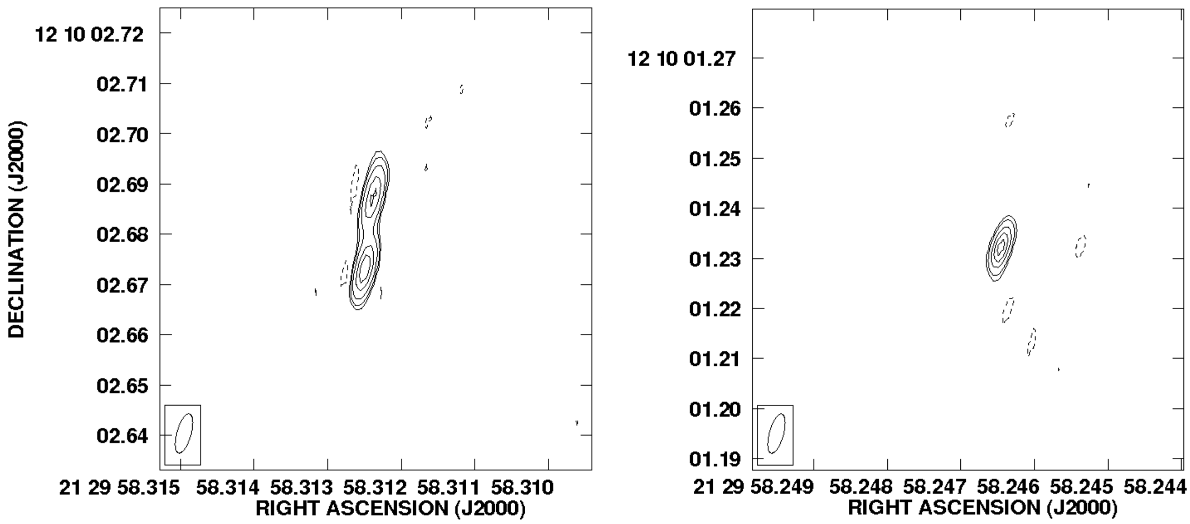

Figure 6.1: Left: Contour plot of AC211 in epoch 3. Contour levels are $(-5,-3,3,5,10,20,30)$ times the rms of 3.6 μJy. Right: Contour plot of 15A in epoch 3 for comparison of the structure. Contour levels are $(-5,-3,3,5,7,10,20)$ times the rms. The beam size and direction is indicated in the bottom left corner of each panel.

per day corresponding to $v \approx$1000 km/s. This velocity is very low compared to measured relativistic jet velocities of, e.g., the X-ray binaries SS433 ($v \sim 0.2$c, Stirling et al. 2002 and references therein) and GRS1915+105 ($v \sim 0.98$c, Fender et al. 1999 and references therein). Therefore, our measured velocity could well be real, especially if the outburst occured at some time close to epoch 2. Turning the argument around, the outburst could have occured only two days before our observations if we assume an ejection velocity of $v \sim 0.2$c.
In Fender et al. 1999 it also becomes clear that the radio flux density of individual components can decrease rapidly on the timescale of a few months. Hence, the time span of 150 days from epoch 3 to 4 is long enough for the ejected material to dissipate and become undetectable again.

6.5 Upper mass limit estimation for the IMBH - candidate in M15

Based on observations of ~100 active galactic nuclei (AGN) in the radio regime at 5 GHz and in the X-ray regime between 2 and 10 keV, Merloni et al. 2003 derived a 'fundamental plane' relating the AGN's black hole mass $M_\bullet$, its X-ray luminosity L_X, and its radio luminosity L_R. In terms of the flux density at 5 GHz F_5 their equation reads

$$F_5 = 10 \left(\frac{L_X}{3 \times 10^{31}\,\mathrm{erg\,s^{-1}}} \right)^{0.6} \left(\frac{M_\bullet}{100\,\mathrm{M_\odot}} \right)^{0.78} \left(\frac{d}{10\,\mathrm{kpc}} \right)^{-2} \mu\mathrm{Jy}\,. \tag{6.2}$$

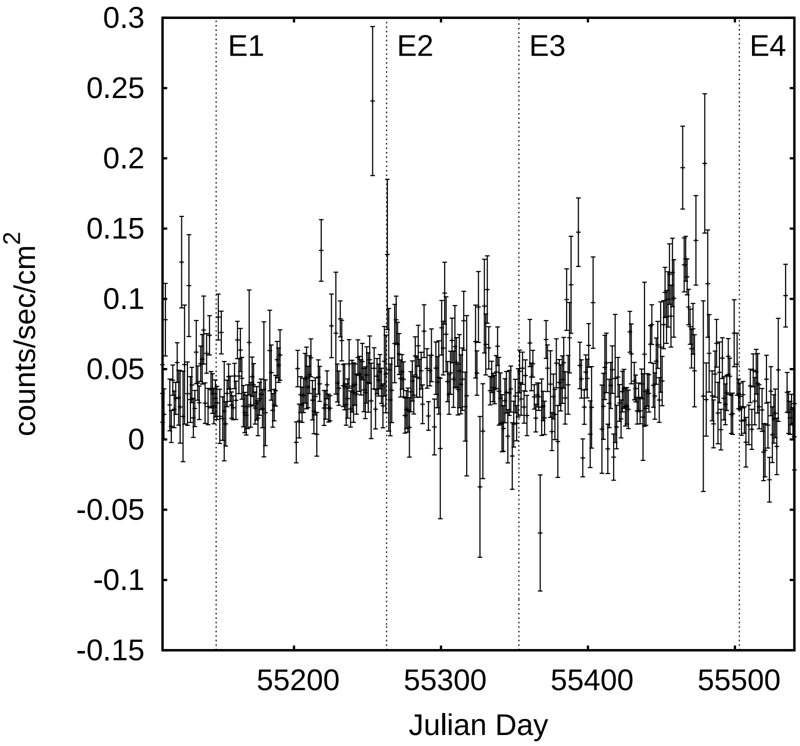

Figure 6.2: Xray light curve of M15 during the observation campaign. The vertical dashed lines indicate the observation day of each epoch. Not the slight increase and sudden drop in photon counts shortly before epoch 3. The data was taken as published by the *MAXI* mission (Matsuoka et al. 2009).

The X-ray luminosity can be expressed in terms of the accretion rate $\dot{M}_{\rm BHL}$

$$L_X = \eta \varepsilon c^2 \dot{M}_{\rm BHL} \,, \tag{6.3}$$

where η and ε are the radiation efficiency and the accretion efficiency, respectively. The radiation efficiency can be expressed as (Maccarone & Servillat 2008)

$$\eta = \frac{0.5\, \varepsilon\, c^2\, \dot{M}_{\rm BHL}}{L_{\rm Edd}} \tag{6.4}$$

where $L_{\rm Edd}$ is the Eddingtion Luminosity. Following Maccarone 2004 we further assume that mass accretion can be described as a Bondi-Hoyle-Lyttleton (BHL) process (Hoyle & Lyttleton 1941, Bondi & Hoyle 1944, Bondi 1952)

$$\dot{M}_{\rm BHL} = 3.2 \times 10^{17} \left(\frac{M_\bullet}{2000\,{\rm M}_\odot}\right)^2 \left(\frac{n}{0.2\,{\rm cm}^{-3}}\right) \left(\frac{T}{10^4{\rm K}}\right)^{-1.5} {\rm g\ s}^{-1} \,. \tag{6.5}$$

Table 6.4: Upper and lower limits of the IMBH mass in M15 for different assumed values of the gas density n and the accretion efficiency ε.

n [$\mathrm{cm^{-3}}$]	$\varepsilon = 0.03$	$\varepsilon = 0.001$
0.42	70 $\mathrm{M_\odot}$	330 $\mathrm{M_\odot}$
0.2	100 $\mathrm{M_\odot}$	470 $\mathrm{M_\odot}$

Here, n and T are the gas density and temperature in the globular cluster, respectively. Combining the above equations, and solving for $M_\bullet$ yields

$$\left(\frac{M_\bullet}{100\,\mathrm{M_\odot}}\right)^{2.6} = 1.32\times10^{-3}\left(\frac{F_5}{\mu\mathrm{Jy}}\right)\left(\frac{d}{10\,\mathrm{kpc}}\right)^2\left[\varepsilon^2\left(\frac{n}{0.2\,\mathrm{cm^{-3}}}\right)\left(\frac{T}{10^4\,\mathrm{K}}\right)^{-3}\right]^{-0.6} . \quad (6.6)$$

We perform the calculations adopting typical values for the temperature $T\sim10^4$ K. To obtain upper and lower limits for the mass of the IMBH we use the values for the gas density as computed by Maccarone & Servillat 2008 (Table 6.4). Furthermore, we set the same upper (lower) limit for the accretion efficiency of $\varepsilon = 0.03$ (0.001) as Maccarone & Servillat 2008. In all calculations we assume a flat radio spectrum and we use the 3σ upper limit of 10 μJy for the flux F. With these values we obtain a mass range of 70-470 $\mathrm{M_\odot}$ (Table 6.4). This result is in agreement with that estimated by Maccarone 2004 who provide a black hole mass of $M_\bullet = 440$ $\mathrm{M_\odot}$.[2] The tight range of our results challenges, however, the mass estimate of Gerssen et al. 2002 (3900 ± 2200 $\mathrm{M_\odot}$, based on a dynamical analysis of stellar motion in M15) and it is still much below even the lower mass limits of Bash et al. 2008 (1000 $\mathrm{M_\odot}$) and Maccarone & Servillat 2010 (700 $\mathrm{M_\odot}$). Therefore, we conclude that M15 either does not host an IMBH (Baumgardt et al. 2003) or that its radio flux density at 1.6 GHz is even below 3 μJy.

[2] This result is based on an estimate of the cluster's total mass, M_{GC}, from its absolute V-magnitude, M_V, and on a model by Miller & Hamilton 2002 stating that $M_\bullet \sim 10^{-3} M_{\mathrm{GC}}$.

7 Conclusions and Outlook

We have presented first results from our multi-epoch observations of M15 at 1.6 GHz with eight antennas from the EVN (including the Arecibo telescope) plus the Greenbank telescope. We have outlined our data reduction procedure and the problems involved. As a major challenge for high astrometric precision in wide field imaging we identify the AIPS task UVFIX to introduce large image registration errors. These occur specifically when shifting the (u, v, w)-coordinates to large angular distances from the phase referencing center (This effect has also been reported by, e.g., Lenc et al. 2008.). Consequently, our positional accuracy is degraded by ~ 1 mas per shift of 10 arcsec in epoch 1.[1] To achieve the highest astrometric precision also for sources further away from the phase referencing center we will explore other shifting algorithms. Morgan et al. 2011 have suggested an algorithm that does not only apply a purely geometric model while shifting the coordinates (like UVFIX does) but that also takes the delay at different positions within the field-of-view into account. We will try and implement this method to reduce the inaccuracy of the positions of 15C, S1, and T169 in epoch 1.

Analyzing the first four of a total of six epochs we measure precise proper motions of the singular pulsar 15A, of the double neutron star 15C, of the low-mass X-ray binary AC211, and of the two unclassified sources S1 and T169. For both 15A and 15C we observe a systematic discrepancy between our astrometric proper motion results and those derived from pulsar timing. Since our results are model independent they can be of great use to improve and confine the pulsar timing solutions, especially the parameters involving the motion of those pulsars within the cluster's gravitational potential. Our observations reveal that the MSP 15C becomes fainter in between epochs and that its flux density drops below the detection threshold in epoch 4 (one year after epoch 1). We interpret its disappearance to be due to geodetic precession causing its beam of emission to move out of our line of sight. As a drawback, we cannot measure the proper motion of 15C with high precision. Later epochs will show whether or not 15C really disappeared or whether it only turned off temporarily. We have performed follow-up observations of M15 at a frequency of 350 MHz with a similar array set-up as the one described here. Expecting the beam width of the MSP to be wider at lower frequencies we might be able to still detect 15C at that frequency.

[1] As of epoch 2 this problem is eliminated by correlating the data at six different positions throughout the FOV.

For the first time, we provide proper motion results for the LMXB AC211 revealing that it really is part of the cluster. In epoch 3 we observe a bipolar morphology of the object which could be caused by a short-term outburst of the source. We have also shown that the flux density of AC211 changes in between epochs and that a similar trend is observable in X-ray observations of the entire cluster. We conclude that the X-ray activity of M15 and the radio brightness of AC211 might be related. Later epochs, however, will need to confirm or reject this hypothesis.

We have shown that our observations are of great help in distinguishing between members of M15 and sources that do not belong to the cluster. Our data proves that S1 follows a trajectory similar to the one of the sources known to be members of M15 and we conclude that S1 is a member of M15 itself. Furthermore, considering its large angular distance from the cluster core, we assume that the motion of S1 is the best indicator for the global motion of M15. Using this result we derive peculiar transverse velocities of 59(17) and 61(20) km/s for 15A and AC211, respectively. These values are above the cluster escape velocity $v_{\rm esc} = 40.9$ km/s (Evans et al. 2003) and could indicate that the sources are slowly leaving the cluster. The remaining two observations of the globular cluster will improve the proper motion results of all sources discussed here and, therefore, we will be able to further constrain the global motion of M15 and the peculiar velocity of sources within the cluster potential.

Our observations provide the first follow-up observations of the unclassified source T169 that was observed previously only once by Knapp et al. 1996. Our data reveals that the object is most likely not part of the cluster since its apparent angular proper motion in declination would imply a peculiar transverse velocity of 536(44) km/s within the cluster. We consider this result to be too large for T169 to be member of M15. This result, however, needs to be reconfirmed in later epochs. Nevertheless, we can confirm that T169 is of Galactic origin.

The flux densities we measure for S1 and T169 vary in between epochs and need to be treated with great care. In general, however, they are consistent with flux density measurements from other authors who also report variability of at least S1 (Knapp et al. 1996). The overall trend of the flux density in dependence on observing frequency implies an almost flat radio spectrum characteristic for optically thick synchrotron emission. We suggest that S1 and T169 could be X-ray binaries that are variable in time. Our follow-up observations at 350 MHz will add to the spectral information of the source helping us to further constrain the nature of the emission mechanism in both S1 and T169.

The high sensitivity of our data set has allowed us to put very tight limits on a possible intermediate mass black hole in M15. Depending on the accretion efficiency and on the actual gas density in the globular cluster we compute a mass range of 70-470 $M_{\odot}$. This range is below most of the previously published estimates for the central IMBH in M15. This could either mean that the IMBH does not emit in the radio regime at 1.6 GHz (at least up to a flux limit of 10 μJy) or that there is no such object altogether. High spacial resolution X-ray observations of the central region of M15 should be able to shed light on this question.

As soon as the remaining two epochs 5 and 6 (and maybe even a seventh epoch) are available we will use the data to confine all results presented here. We will also continue our search for new sources by cross-checking positions of candidates for new detections in between epochs. Furthermore, we will address another aim of this project which is to measure a curvature in the proper motion of the compact radio objects known to be members of M15. From this curvature we will be able to derive the orbit of those sources about the central mass concentration which, in turn, will enable us to give an estimate on the central mass of M15. Thereby, we will add evidence to the existence or non-existence of an IMBH as the central mass concentration in M15.

Epoch 6 has been observed in June 2011. In contrast to all other epochs, the raw data from the individual telescopes will be kept after correlation. We will use this data to achieve a number of things. The main aim of keeping the raw data from epoch 6 deals with the implementation of a correlation algorithm providing a temporal resolution of the data on the order of milliseconds. Such a correlated dataset would have a much higher sensitivity than any of the individual telescopes and could be used to perform standard pulse searches via time folding. Since the pulse frequency of the pulsar 15A is known, we will use the data of the observations of M15 as a test bed for the algorithm. As a next step we will search for pulses in S1 and T169 to draw conclusions about their nature. A further goal of keeping the raw data is to combine the data of all telescopes to obtain highest sensitivity. In this stacked data we might be able to detect 15C once again and follow its motion across the sky. Another possibility is to employ pulsar gating during a second correlation run at the position of 15C. For this to work properly, however, we will need to extrapolate the last known timing solutions to the observing time of epoch 6.

On the long-term, we intend to observe further globular clusters and the Galactic center to search for compact radio sources that could turn out to be pulsars. In this search, the algorithm we will implement will be of great help. Multi-epoch, high sensitivity observations with high spacial resolution have the potential to detect faint sources that can be used as test particles in the gravitational field of compact objects to study fundamental physics. In case of globular cluster they are of help to investigate cluster dynamics and to shed light on the nature of the central source. If we are able to detect compact objects such as millisecond pulsars close to the Galactic center we will contribute to tests of different theories of gravity.

8 Acknowledgement

My greatest thanks go to my supervisor Dr. Wouter Vlemmings who suggested the topic and led me through this thesis. I very much appreciate his patience and constant support at all times.

Furthermore, I would like to thank Prof. Dr. Michael Kramer and Prof. Dr. Norbert Langer for accepting my request to be first and second referee, respectively. I appreciate Paulo Freire's input about the effects of geodetic precession and I am grateful for discussions about X-ray binaries with Anthony Rushton.

I acknowledge financial support by the Bonn Cologne Graduate School of Physics and Astronomy. This research has made use of the MAXI data provided by RIKEN, JAXA and the MAXI team.

Bibliography

Abdo, A. A., et al. 2009, Science, 325, 84

Anderson, S. B., Gorham, P. W., Kulkarni, S. R., Prince, T. A., & Wolszczan, A. 1990, Nature, 346, 42

Barker, B. M., & O'Connell, R. F. 1975, ApJL, 199, L25

Bash, F. N., Gebhardt, K., Goss, W. M., & Vanden Bout, P. A. 2008, AJ, 135, 182

Batten, A. H. 1967, ARAA, 5, 25

Baumgardt, H., Hut, P., Makino, J., McMillan, S., & Portegies Zwart, S. 2003, ApJL, 582, L21

Boboltz, D. A., Gaume, R. A., Fey, A. L., Ma, C., Gordon, D., & IERS/IVS Working Group on ICRF2 2010, Bulletin of the American Astronomical Society, 42, #469.06

Bondi, H. 1952, MNRAS, 112, 195

Bondi, H., & Hoyle, F. 1944, MNRAS, 104, 273

Briggs, D. S., Schwab, F. R., & Sramek, R. A. 1999, Synthesis Imaging in Radio Astronomy II, 180, 127

Camilo, F., Lorimer, D. R., Freire, P., Lyne, A. G., & Manchester, R. N. 2000, ApJ, 535, 975

Charles, P. A., Clarkson, W. I., & van Zyl, L. 2002, New Astronomy, 7, 21

Cordes, J. M., & Lazio, T. J. W. 2003, arXiv:astro-ph/0301598

Djorgovski, S., & King, I. R. 1986, ApJL, 305, L61

Evans, A., Stickel, M., van Loon, J. T., Eyres, S. P. S., Hopwood, M. E. L., & Penny, A. J. 2003, A&A, 408, L9

Fender, R. P., Garrington, S. T., McKay, D. J., Muxlow, T. W. B., Pooley, G. G., Spencer, R. E., Stirling, A. M., & Waltman, E. B. 1999, MNRAS, 304, 865

Fey, A. L., et al. 2004, AJ, 127, 3587

Freire, P. C., Camilo, F., Kramer, M., Lorimer, D. R., Lyne, A. G., Manchester, R. N., & D'Amico, N. 2003, MNRAS, 340, 1359

Gerssen, J., van der Marel, R. P., Gebhardt, K., Guhathakurta, P., Peterson, R. C., & Pryor, C. 2002, AJ, 124, 3270

Graham-Smith, F. 2003, Reports on Progress in Physics, 66, 173

Hewish, A., Bell, S. J., Pilkington, J. D. H., Scott, P. F., & Collins, R. A. 1968, Nature, 217, 709

Högbom, J. A. 1974, A&AS, 15, 417

Hotan, A. W., Bailes, M., & Ord, S. M. 2005, ApJ, 624, 906

Hoyle, F., & Lyttleton, R. A. 1941, MNRAS, 101, 227

Jacoby, B. A., Cameron, P. B., Jenet, F. A., Anderson, S. B., Murty, R. N.,

Koch, A., & McWilliam, A. 2011, AJ, 142, 63 & Kulkarni, S. R. 2006, Bulletin of the American Astronomical Society, 38, 1027

Janka, H.-T., Langanke, K., Marek, A., Martínez-Pinedo, G., Müller, B. 2007, Physics Reports, 442, 38

Johnston, H. M., Kulkarni, S. R., & Goss, W. M. 1991, ApJ, 382, L89

Knapp, G. R., Gunn, J. E., Bowers, P. F., & Vasquez Poritz, J. F. 1996, ApJ, 462, 231

Kramer, M. 1998, ApJ, 509, 856

Kramer, M, & Wex, N. 2009, Classical and Quantum Gravity, 26, 073001

Lenc, E., Garrett, M. A., Wucknitz, O., Anderson, J. M., & Tingay, S. J. 2008, ApJ, 673, 78

Lorimer, D. R., & Kramer, M. 2005, Handbook of Pulsar Astronomy, Cambridge University Press

Lorimer, D. R. 2008, Living Reviews in Relativity, 11, 8

Lu, T.-N., & Kong, A. K. H. 2011, ApJL, 729, L25

Lyne, A. G., & Graham-Smith, F. 1998, Pulsar astronomy

Maccarone, T. J. 2004, MNRAS, 351, 1049

Maccarone, T. J., & Servillat, M. 2008, MNRAS, 389, 379

Maccarone, T. J., & Servillat, M. 2010, MNRAS, 408, 2511

Machin, G., Lehto, H. J., McHardy, I. M., Callanan, P. J., & Charles, P. A. 1990, MNRAS, 246, 237

Manchester, R. N., Hobbs, G. B., Teoh, A., & Hobbs, M. 2005, AJ, 129, 1993

Manchester, R. N., Kramer, M., Stairs, I. H., Burgay, M., Camilo, F., Hobbs, G. B., Lorimer, D. R., Lyne, A. G., McLaughlin, M. A., McPhee, C. A., Possenti, A., Reynolds, J. E., & van Straten, W. 2010, ApJ, 710, 1694

Maron, O., Kijak, J., Kramer, M., & Wielebinski, R. 2000, A&AS, 147, 195

Matsuoka, M., et al. 2009, PASJ, 61, 999

McNamara, B. J., Harrison, T. E., & Baumgardt, H. 2004, ApJ, 602, 264

Merloni, A., Heinz, S., & di Matteo, T. 2003, MNRAS, 345, 1057

Migliari, S., et al. 2010, ApJ, 710, 117

Miller, M. C., & Hamilton, D. P. 2002, MNRAS, 330, 232

Miocchi, P. 2010, A&A, 514, A52

Morgan, J. S., Mantovani, F., Deller, A. T., Brisken, W., Alef, W., Middelberg, E., Nanni, M., & Tingay, S. J. 2011, A&A, 526, A140

Pacini, F. 1967, Nature, 216, 567

Y Potekhin, A. 2010, Physics Uspekhi, 53, 1235

Ransom, S. M., Hessels, J. W. T., Stairs, I. H., Freire, P. C. C., Camilo, F., Kaspi, V. M., &

Kaplan, D. L. 2005, Science, 307, 892

Ryle, M., & Vonberg, D. D. 1946, Nature, 158, 339

Saz Parkinson, P. M., et al. 2010, ApJ, 725, 571

Schilizzi, R. T., et al. 2001, Experimental Astronomy, 12, 49

Schwab, F. R. 1984, AJ, 89, 1076

Sneden, C., Kraft, R. P., Shetrone, M. D., Smith, G. H., Langer, G. E., & Prosser, C. F. 1997, AJ, 114, 1964

Sovers, O. J., Fanselow, J. L., & Jacobs, C. S. 1998, Reviews of Modern Physics, 70, 1393

Stirling, A. M., Jowett, F. H., Spencer, R. E., Paragi, Z., Ogley, R. N., & Cawthorne, T. V. 2002, MNRAS, 337, 657

Sun, X.-H., Han, J.-L., & Qiao, G.-J. 2002, ChJAA, 2, 133

Thompson, A. R., Moran, J. M., & Swenson, G. W. 1986, ISRN Astronomy and Astrophysics

Thompson, A. R. 1999, Synthesis Imaging in Radio Astronomy II, 180, 11

van der Marel, R. P. 2003, Bulletin of the American Astronomical Society, 35, 1370

Vlemmings, W. H. T., Cordes, J. M., & Chatterjee, S. 2004, ApJ, 610, 402

Walker, R. C., & Chatterjee, S. 1999, VLBA Scientific Memo 23 (Socorro, NM: NRAO), `http://www.vlba.nrao.edu/memos/sci/`

Weisberg, J. M., Romani, R. W., & Taylor, J. H. 1989, ApJ, 347, 1030

I hereby certify that the work presented here was accomplished by myself and without the use of illegitimate means or support, and that no sources and tools were used other than those cited.

Bonn, …………………… ……………………………….

Date Signature